

Multipartite Dark Matter with Scalars, Fermions and signatures at LHC

Subhaditya Bhattacharya,^a Purusottam Ghosh,^a Narendra Sahu^b

^a*Department of Physics, Indian Institute of Technology Guwahati, North Guwahati, Assam- 781039, India*

^b*Department of Physics, Indian Institute of Technology Hyderabad, Kandi, Sangareddy, Telangana- 502285, India*

E-mail: subhab@iitg.ac.in, pghoshiitg@gmail.com, nsahu@iith.ac.in

ABSTRACT: Basic idea of this analysis is to achieve a two-component dark matter (DM) framework composed of a scalar and a fermion, with non-negligible DM-DM interaction contributing to thermal freeze out (hence relic density), but hiding them from direct detection bounds. We therefore augment the Standard Model (SM) with a scalar singlet (S) and three vectorlike fermions: two singlets (χ_1, χ_2) and a doublet (N). Stability of the two DM components is achieved by a discrete $\mathcal{Z}_2 \times \mathcal{Z}'_2$ symmetry, under which the additional fields transform suitably. Fermion fields having same $\mathcal{Z}_2 \times \mathcal{Z}'_2$ charge (N, χ_1 in the model) mix after electroweak symmetry breaking (EWSB) and the lightest component becomes one of the DM candidates, while scalar singlet S is the other DM component connected to visible sector by Higgs portal coupling. The heavy fermion (χ_2) plays the role of mediator to connect the two DM candidates through Yukawa interaction. This opens up a large parameter space for the heavier DM component through DM-DM conversion. Hadronically quiet dilepton signature, arising from the fermion dark sector, can be observed at Large Hadron Collider (LHC) aided by the presence of a lighter scalar DM component, satisfying relic density and direct search bounds through DM-DM conversion.

Contents

1	Introduction	1
2	The Model	3
2.1	Constraints on the model parameters	8
2.2	Possible multipartite DM scenarios	9
3	Review of single component DM frameworks with N_1 and S	10
3.1	Single component fermion DM (N_1)	10
3.2	Single component scalar DM (S)	11
4	Two Component DM with N_1 and S	12
4.1	Coupled Boltzmann Equations	13
4.2	Relic density and direct search outcome	15
5	Two Component DM in presence of additional heavy scalar	24
6	Collider searches at LHC	27
7	Possible implications to Inflation and Reheating	36
8	Summary	37
A	Single Component vector-like fermion DM	38
B	Higgs Invisible Decay Constraint	41
C	Invisible Decay Constraint of Z	42

1 Introduction

Observation of galactic rotation curves [1, 2], gravitational lensing and anisotropies in cosmic microwave background [3] collectively hint towards the existence of a cosmologically stable dark matter (DM) component in the the present Universe [4]. However, there is no such particle candidate exist within the standard model (SM), which can behave as DM. Hence physics beyond the SM is inevitable. Hitherto the only information known about DM is its relic abundance and is precisely determined by Wilkinson Microwave Anisotropy Probe (WMAP) [5] and PLANCK [6] to be $\Omega_{\text{DM}}h^2 = 0.1161 \pm 0.0028$. Apart from this, we don't have any other information about DM, such as its mass, spin, interaction *etc.* As a result, the nature of DM being a scalar, a fermion, or a vector boson or an admixture of them can not be avoided. In addition to gravity, if the DM is weakly interacting to

visible sector, then it can thermalise in the early Universe at a temperature above its mass scale. As the Universe cools down due to Hubble expansion, the DM freezes-out from the thermal plasma at a temperature below its mass scale and gets redshifted since then. It is miraculous that the observed DM abundance implies to thermal freeze-out cross-section of DM: $\langle\sigma|v|\rangle \approx 10^{-36}\text{cm}^2$, of typical weak interaction strength and therefore it is largely believed that the DM is a weakly interacting massive particle (WIMP) [7].

However, the WIMP paradigm suffers from a serious threat due to the non-observation of DM in direct search experiments. In fact, in a few years from now the DM-nucleon cross-section measured at direct search experiments may hit the neutrino floor [8], where neutrino-nucleon cross-section will be a huge background for DM detection. The main problem in a WIMP paradigm is that the interactions which lead to the freeze-out of DM in the early Universe, also yields DM-nucleon cross-section in direct search experiments in the present epoch, such as LUX [9], XENON [10, 11], PANDA [12] *etc.* The same is true for non-observation of DM in collider searches as well. The only difference for a WIMP of ~ 100 GeV is that the production of DM at collider is suppressed (with no electromagnetic or strong interactions with SM), so that non-observation of DM in collider provides less constraint than those of direct searches at terrestrial laboratories.

Multipartite DM frameworks [13–30] can provide a cushion to the tension of WIMP like particles to satisfy simultaneously relic density and direct search constraints. This is essentially due to some processes which can still contribute to the depletion of DM number density for thermal freeze-out, but do not contribute to direct search cross-sections. The main two contributions of such kind can arise from: (i) Co-annihilation of DM with a heavier particle, which can not be produced in direct search for kinematic suppression [21, 31] or (ii) DM-DM interactions, where the heavier DM component can annihilate to the lighter one to yield thermal relic, but do not contribute to direct searches of DM [20, 21].

Our paper investigates one of the simplest of such cases, where we assume the presence of two DM components: one scalar (S) and a fermion (N_1). While both DMs have been studied as individual components [21, 32–34], we study the interplay of DM-DM interactions when they are present together. In order to enhance such interactions, we insert an additional singlet fermion field (χ_2), which works as a mediator and carries the interaction through a Yukawa term. We thereafter demonstrate that a large parameter space becomes available to each DM components, whichever is heavy, saved from direct search bound thanks to enhanced DM-DM interactions. The lighter DM component however, has the fate similar to that of a single component case, particularly when direct search is concerned. This shows that scalar DM can only be present in the vicinity of Higgs resonance ($m_S \sim m_h/2$) when it is lighter than fermion DM. The presence of an additional heavy scalar (S_H) in the model can however yield a larger parameter space for the scalar DM (even when it is lighter than fermion DM). Efforts have already been made to accommodate scalar and fermion DM together in a single framework [14, 17], but most often the role of DM-DM interactions has been subdued and the outcome is predictive and severely constrained.

Collider signatures of both the DM components have also been addressed before (see for example, [35, 36]). Unfortunately, it turns out that neither the scalar nor the fermion

DM (in their single component realisation) has a possibility of producing signal excess over SM background in near future run of Large Hadron Collider (LHC)¹, while satisfying relic density and direct search constraints. We however demonstrate here, the presence of a lighter scalar DM component helps in identifying hadronically quiet dilepton signal (a characteristic signature for the charged lepton components present in the fermion dark sector) at LHC, which was otherwise impossible due to unsurpassable SM background contribution. This is accessible due to the freedom of utilising a larger missing energy cut, resulting from a larger allowed mass difference between the fermion DM and its charge companions, thanks to the presence of a lighter DM component and non-negligible DM-DM interactions in the set up to satisfy relic density and direct search bounds.

The paper is organised as follows. We first introduce the model framework (in Section 2). After reviewing relic density and direct search constraints on the individual DM components for single component frameworks (in Section 3), we discuss in details the case of two-component set up poised with DM-DM conversion (in Section 4). We also point out to the possibilities of having an additional heavy scalar in the framework (in Section 5). We then elucidate signatures of fermion dark sector at LHC accessible through two component set up (in Section 6). We also briefly discuss possible cosmological effect on DM particles due to early universe inflation and reheating (in Section 7). Finally we summarise and conclude (in Section 8). Some illustrative features of fermion DM, Higgs invisible decay and Z invisible decay constraints on the model are detailed in Appendices A, B and C respectively.

2 The Model

The model addressed here, accommodates two single component DM frameworks together: (i) a real scalar singlet DM (S), connected to SM through Higgs portal [21, 32, 33, 37] and (ii) a fermion DM arising out of the admixture of vectorlike fermion (VF) doublet, $N = \begin{pmatrix} N^0 & N^- \end{pmatrix}^T$ and a vectorlike fermion singlet χ_1 [34, 35, 38], where lightest component becomes a DM. Stability of a single DM can be ensured by an additional discrete \mathbb{Z}_2 symmetry, under which the DM transforms nontrivially. However, when two DMs are present together, the stability of both components can be ensured by enhancing the symmetry to $\mathbb{Z}_2 \times \mathbb{Z}_2'$, where two DMs transform differently under the symmetry as we will illustrate shortly. Two-component DM frameworks are naturally disfavoured from direct search as each DM component acquires smaller relic density resulting enhanced annihilation cross-section to SM for freeze out. This enhances direct search cross-sections for both the DM components (resulting from same interaction vertices). This is the reason that most of the existing scalar-fermion DM scenarios have been severely discarded by stringent direct search limits [14, 17]. However, DM-DM interactions may come to rescue as the freeze-out of the heavier component will then be additionally driven by its annihilation to lighter DM component, which do not contribute to direct search cross-section of that component. In order to enhance such interplay, we have introduced an additional vectorlike

¹Fermion DM with singlet-doublet mixing may however yield a displaced vertex signature [35].

singlet fermion χ_2 , which behaves like a messenger between the two DM components. The interaction between the two DM components and their individual connection to the visible sector (SM) are shown by a schematic diagram in Fig. 1. Under the $\mathcal{Z}_2 \times \mathcal{Z}'_2$ symmetry, additional dark fields transform as: N $[-, +]$, χ_1 $[-, +]$, χ_2 $[+, -]$ and S $[-, -]$, where all SM fields remain invariant: SM $[+, +]$. The quantum numbers under the SM gauge group $SU(3)_C \times SU(2)_L \times U(1)_Y$ and $\mathcal{Z}_2 \times \mathcal{Z}'_2$ symmetry for these additional fields are shown in the Table 1. It is remarkable that these additional fermions χ_1 , χ_2 and N are vector-like and hence they don't introduce any extra anomalies. This is easy to see through the chiral gauge anomaly free condition coming from the one loop triple gauge boson vertex, which reads [39]:

$$\sum_{rep} Tr[\{T_L^a, T_L^b\}T_L^c] - Tr[\{T_R^a, T_R^b\}T_R^c] = 0. \quad (2.1)$$

Here, T denotes the generators for the SM gauge group and L, R denotes the interactions of left or right chiral fermions with the gauge bosons. It is straightforward to see, that while the SM satisfies the anomaly free condition because of the presence of a quark family to each lepton family [39, 40], the additional vector like fermions introduced here, have the left chiral components transforming similarly to the right chiral ones under the SM gauge symmetry. Therefore, the model is anomaly free.

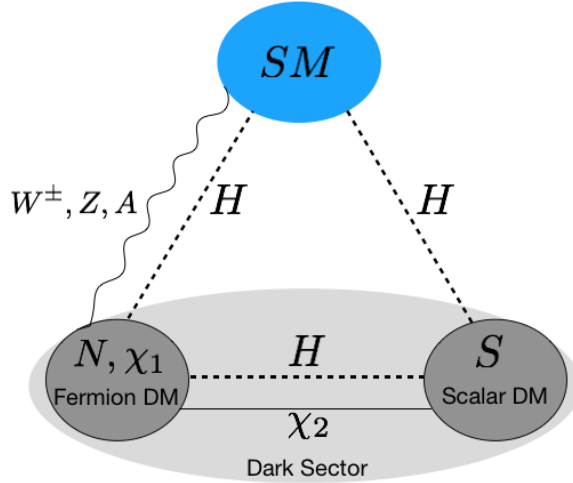


Figure 1: Schematic diagram showing the interactions between scalar and fermion DM components and that to SM particles.

In Table 1, we note that N and χ_1 have similar $\mathcal{Z}_2 \times \mathcal{Z}'_2$ charges. Hence they mix with each other after the SM Higgs acquires a vacuum expectation value (vev), while the other fermion χ_2 does not. The lightest of such singlet-doublet admixture can be one fermion DM component of this model. The scalar singlet S also have different charge assignment from that of all the other fermion fields, allowing it to be stabilized to form another DM component. The key feature of this model is the possibility of writing a Yukawa interaction

Dark Fields	$\underbrace{SU(3)_C \times SU(2)_L \times U(1)_Y}_{\mathcal{G}} \times \mathcal{Z}_2 \times \mathcal{Z}'_2$				
$N = \begin{pmatrix} N^0 \\ N^- \end{pmatrix}$	1	2	-1	-	+
χ_1	1	1	0	-	+
χ_2	1	1	0	+	-
S	1	1	0	-	-

Table 1: Dark sector fields and their corresponding quantum numbers under $\mathcal{G} \equiv SU(3)_C \times SU(2)_L \times U(1)_Y \times \mathcal{Z}_2 \times \mathcal{Z}'_2$.

between χ_1, χ_2 , and S by the assigned $\mathcal{Z}_2 \times \mathcal{Z}'_2$ charges, which adds to the possible DM-DM interactions as we explain below. This particular feature segregates this model from earlier attempts of two component scalar-fermion DM set-up like in [14, 17], where DM-DM interactions were small, so the model becomes strongly constrained by direct search or from the case where fermion DM doesn't have an interaction with visible sector (excepting at the loop level) to credit a large share of relic density to it and thus constraining the model to a particular possibility.

Let us now describe the Lagrangian for the model, which can be segregated into three parts, constituting the vector like fermion sector, scalar sector and the interaction between the fermion and scalar sector as follows:

$$\mathcal{L} \supset \mathcal{L}^{VF} + \mathcal{L}^{Scalar} + \mathcal{L}^{VF+Scalar}, \quad (2.2)$$

where,

$$\begin{aligned} \mathcal{L}^{VF} = & \bar{N} \left[i\gamma^\mu (\partial_\mu - ig \frac{\sigma^a}{2} W_\mu^a - ig' \frac{Y'}{2} B_\mu) - m_N \right] N \\ & + \bar{\chi}_1 (i\gamma^\mu \partial_\mu - m_{\chi_1}) \chi_1 - (Y_1 \bar{N} \tilde{H} \chi_1 + h.c) \\ & + \bar{\chi}_2 (i\gamma^\mu \partial_\mu - m_{\chi_2}) \chi_2, \end{aligned} \quad (2.3)$$

$$\mathcal{L}^{Scalar} = \frac{1}{2} \partial^\mu S \partial_\mu S - \frac{1}{2} m_S^2 S^2 - \frac{1}{4!} \lambda_S S^4 - \frac{1}{2} \lambda_{SH} \left(H^\dagger H - \frac{v^2}{2} \right) S^2, \quad (2.4)$$

and

$$\mathcal{L}^{VF+Scalar} = -Y_2 (\bar{\chi}_1 \chi_2 S + h.c). \quad (2.5)$$

There are two Yukawa interactions present in this model. We will focus on the first in Eqn. 2.3. Electroweak symmetry breaking (EWSB) occurs as the SM Higgs acquires a vacuum expectation value: $H = \left(0 \quad \frac{1}{\sqrt{2}}(v+h) \right)^T$ where $v = 246$ GeV. The Yukawa $Y_1 \bar{N} \tilde{H} \chi_1$ term in the Lagrangian (Eqn. 2.3) mixes N^0 and χ_1 . Mass terms of the vector like fermions in \mathcal{L}^{VF} then take the following form:

$$\begin{aligned}
-\mathcal{L}_{mass}^{VF} &= m_N \overline{N^0} N^0 + m_N N^+ N^- + m_{\chi_1} \overline{\chi_1} \chi_1 + \frac{Y_1 v}{\sqrt{2}} \overline{N^0} \chi_1 + \frac{Y_1 v}{\sqrt{2}} \overline{\chi_1} N^0 \\
&= \overline{\begin{pmatrix} \chi_1 & N^0 \end{pmatrix}} \begin{pmatrix} m_{\chi_1} & \frac{Y_1 v}{\sqrt{2}} \\ \frac{Y_1 v}{\sqrt{2}} & m_N \end{pmatrix} \begin{pmatrix} \chi_1 \\ N^0 \end{pmatrix} + m_N N^+ N^- \\
&= \overline{\begin{pmatrix} N_1 & N_2 \end{pmatrix}} \begin{pmatrix} m_1 & 0 \\ 0 & m_2 \end{pmatrix} \begin{pmatrix} N_1 \\ N_2 \end{pmatrix} + m_N N^+ N^-, \tag{2.6}
\end{aligned}$$

where in the last step, the unphysical basis, $\begin{pmatrix} \chi_1 & N^0 \end{pmatrix}^T$ is related to physical basis, $\begin{pmatrix} N_1 & N_2 \end{pmatrix}^T$ through the following unitary transformation:

$$\begin{pmatrix} \chi_1 \\ N^0 \end{pmatrix} = \mathcal{U} \begin{pmatrix} N_1 \\ N_2 \end{pmatrix} = \begin{pmatrix} \cos \theta & -\sin \theta \\ \sin \theta & \cos \theta \end{pmatrix} \begin{pmatrix} N_1 \\ N_2 \end{pmatrix}, \tag{2.7}$$

where the mixing angle

$$\tan 2\theta = -\frac{\sqrt{2}Y_1 v}{m_N - m_{\chi_1}}. \tag{2.8}$$

The mass eigenvalues of the physical states N_1 and N_2 , for small $\sin \theta$ ($\sin \theta \rightarrow 0$) limit, can be expressed as:

$$\begin{aligned}
m_{N_1} &\simeq m_{\chi_1} + \frac{Y_1 v}{\sqrt{2}} \sin 2\theta \equiv m_{\chi_1} - \frac{(Y_1 v)^2}{(m_N - m_{\chi_1})}, \\
m_{N_2} &\simeq m_N - \frac{Y_1 v}{\sqrt{2}} \sin 2\theta \equiv m_N + \frac{(Y_1 v)^2}{(m_N - m_{\chi_1})}. \tag{2.9}
\end{aligned}$$

Here we have considered $Y_1 v / \sqrt{2} < m_{\chi_1} < m_N$. Hence $m_{N_1} < m_{N_2}$. Therefore N_1 becomes the stable DM candidate (with a small kinematic caveat as we discuss shortly). Using Eqn. 2.8, one can find:

$$\begin{aligned}
Y_1 &= -\frac{\Delta m \sin 2\theta}{\sqrt{2}v}, \\
m_N &= m_{N_1} \sin^2 \theta + m_{N_2} \cos^2 \theta. \tag{2.10}
\end{aligned}$$

where $\Delta m = m_{N_2} - m_{N_1}$ is the mass difference between the two mass eigenstates and m_N is the mass of electrically charged component of vectorlike fermion doublet N^\mp . This serves as an important parameter for the phenomenology of the model as we illustrate. Note again that due to a different $\mathcal{Z}_2 \times \mathcal{Z}'_2$ charge, χ_2 do not mix with N and χ_1 .

Vector like fermion DM has gauge interactions to SM due to the inclusion of doublet in the model. Expanding the covariant derivative in \mathcal{L}^{VF} , one can find:

$$\mathcal{L}_{int}^{VF} = \overline{N} i \gamma^\mu \left(-ig \frac{\sigma^a}{2} W_\mu^a + i \frac{g'}{2} B_\mu \right) N$$

$$\begin{aligned}
&= \left(\frac{e_0}{2 \sin \theta_W \cos \theta_W} \right) \overline{N^0} \gamma^\mu Z_\mu N^0 + \frac{e_0}{\sqrt{2} \sin \theta_W} \overline{N^0} \gamma^\mu W_\mu^+ N^- + \frac{e_0}{\sqrt{2} \sin \theta_W} N^+ \gamma^\mu W_\mu^- N^0 \\
&\quad - e_0 N^+ \gamma^\mu A_\mu N^- - \left(\frac{e_0}{2 \sin \theta_W \cos \theta_W} \right) \cos 2\theta_W N^+ \gamma^\mu Z_\mu N^-
\end{aligned} \tag{2.11}$$

where $g = e_0/\sin \theta_W$ and $g' = e_0/\cos \theta_W$ with e_0 being the electromagnetic coupling constant and θ_W being the Weinberg angle. One can therefore express the gauge and the Yukawa interactions of \mathcal{L}^{VF} in mass basis of N_1 and N_2 as:

$$\begin{aligned}
\mathcal{L}_{int}^{VF} = & \left(\frac{e_0}{2 \sin \theta_W \cos \theta_W} \right) \left[\sin^2 \theta \overline{N_1} \gamma^\mu Z_\mu N_1 + \cos^2 \theta \overline{N_2} \gamma^\mu Z_\mu N_2 \right. \\
& \quad \left. + \sin \theta \cos \theta (\overline{N_1} \gamma^\mu Z_\mu N_2 + \overline{N_2} \gamma^\mu Z_\mu N_1) \right] \\
& + \frac{e_0}{\sqrt{2} \sin \theta_W} \sin \theta \overline{N_1} \gamma^\mu W_\mu^+ N^- + \frac{e_0}{\sqrt{2} \sin \theta_W} \cos \theta \overline{N_2} \gamma^\mu W_\mu^+ N^- \\
& + \frac{e_0}{\sqrt{2} \sin \theta_W} \sin \theta N^+ \gamma^\mu W_\mu^- N_1 + \frac{e_0}{\sqrt{2} \sin \theta_W} \cos \theta N^+ \gamma^\mu W_\mu^- N_2 \\
& - e_0 N^+ \gamma^\mu A_\mu N^- - \left(\frac{e_0}{2 \sin \theta_W \cos \theta_W} \right) \cos 2\theta_W N^+ \gamma^\mu Z_\mu N^- \\
& - \frac{Y_1}{\sqrt{2}} h \left[\sin 2\theta (\overline{N_1} N_1 - \overline{N_2} N_2) + \cos 2\theta (\overline{N_1} N_2 + \overline{N_2} N_1) \right]
\end{aligned} \tag{2.12}$$

Let us now focus into the other Yukawa interaction between different DM particles as introduced in $\mathcal{L}^{VF+Scalar}$ (Eqn. 2.5). In the physical basis it reads:

$$\mathcal{L}_{int}^{VF+Scalar} = -Y_2 (\cos \theta \overline{N_1} \chi_2 S - \sin \theta \overline{N_2} \chi_2 S + \cos \theta \overline{\chi_2} N_1 S - \sin \theta \overline{\chi_2} N_2 S). \tag{2.13}$$

The scalar field S do not acquire any vev and thus retains the $\mathcal{Z}_2 \times \mathcal{Z}'_2$ symmetry intact and is eligible as a possible DM candidate of the model. The interaction terms involving S of \mathcal{L}^{Scalar} after EWSB turns out to be:

$$\mathcal{L}_{int}^{Scalar} = -\frac{\lambda_{SH} v}{2} h S^2 - \frac{\lambda_{SH}}{4} h^2 S^2. \tag{2.14}$$

Following \mathcal{L}^{Scalar} (Eqn. 2.4), the full scalar potential including SM Higgs can be written as:

$$V(H, S) = -\mu_H^2 (H^\dagger H) + \lambda_H (H^\dagger H)^2 + \frac{1}{2} m_S^2 S^2 + \frac{\lambda_S}{4!} S^4 + \frac{\lambda_{SH}}{2} \left(H^\dagger H - \frac{v^2}{2} \right) S^2. \tag{2.15}$$

It is important now to identify the key parameters of the model which control relevant phenomenology of the model. Mainly seven independent parameters do the job including two DM masses, mass of the mediator, mixing angle of singlet-doublet fermion, Yukawa coupling denoting DM-DM interactions and the Higgs portal coupling of the scalar DM respectively:

$$\{ m_{N_1}, \Delta m, m_S, m_{\chi_2}, \sin \theta, Y_2, \lambda_{SH} \} \tag{2.16}$$

2.1 Constraints on the model parameters

Before evaluating the constraints on the model parameters given in Eqn. 2.16, from DM and collider analysis, we would like to go through the constraints coming from stability of the potential, perturbativity of the parameters and invisible decay widths of Z and H to determine the broad parameter space available for our numerical scan.

- **Stability of potential:** For the tree-level vacuum stability of the scalar potential as in Eqn. (2.15), one requires to satisfy the following co-positivity conditions [41]:

$$\lambda_H \geq 0, \quad \lambda_S \geq 0, \quad \text{and} \quad \lambda_{SH} + \sqrt{\frac{2}{3}\lambda_H \lambda_S} \geq 0. \quad (2.17)$$

This essentially means, we satisfy the constraints if we assume $\lambda_H, \lambda_S, \lambda_{SH} \geq 0$ throughout the scan.

- **Perturbativity:** The upper limit of perturbativity bound on quartic and Yukawa couplings of the model are given by,

$$|\lambda_S|, |\lambda_{SH}| < 4\pi, \\ \text{and} \quad |Y_1|, |Y_2| < \sqrt{4\pi}. \quad (2.18)$$

- **Relic density of DM:** The total relic density of DM is limited by the combined WMAP [5] and PLANCK [6] data as:

$$\Omega_{\text{DM}} h^2 = 0.1161 \pm 0.0028. \quad (2.19)$$

- **Invisible decay width of Higgs :** Invisible Higgs decay width puts strong constraints on light DM having masses $< m_h/2$ if they are connected through Higgs portal, as we have in the model. Current bound from LHC on Higgs invisible branching fraction is given by [42]:

$$\text{Br} (\text{Higgs} \rightarrow \text{inv.}) < 0.24. \quad (2.20)$$

Details have been furnished in Appendix B.

- **Invisible decay width of Z :** Z boson can decay to DM with $m_{DM} < M_Z/2$, whenever the DM has a weak charge as is the case for the fermion DM component of the model. Invisible decay of Z is strongly constrained from observable data. The upper limit of invisible Z decay width is [42]:

$$\Gamma(Z \rightarrow \text{inv.}) \leq 499 \pm 1.5 \text{ MeV}. \quad (2.21)$$

One may find the details about this constraint applied to our case in Appendix C.

2.2 Possible multipartite DM scenarios

We have four electromagnetic charge neutral particles in the model: N^0 , χ_1 , χ_2 and S . Given the same charge of N^0 and χ_1 under $\mathcal{Z}_2 \times \mathcal{Z}_2'$, they mix and the lighter eigenstate N_1 (with $m_{N_1} < m_{N_2}$) can not decay to SM, while N_2 decays to N_1 . Then, we are left with three possible DM candidates, i.e. N_1 , χ_2 and S . However, the absolute stability will be dictated by other Yukawa coupling present in dark sector $Y_2 \overline{\chi_1} \chi_2 S \rightarrow Y_2 \overline{N_1} \chi_2 S$ (as in Eqn. 2.13). Evidently, if one of the physical states is heavier than the other two, then it can decay to the other two lighter particles and become unstable. As a result, the two lighter physical states will be the viable DM candidates. Therefore, depending on the mass hierarchy, the model offers four different types of multipartite DM scenarios as illustrated in Fig. 2.

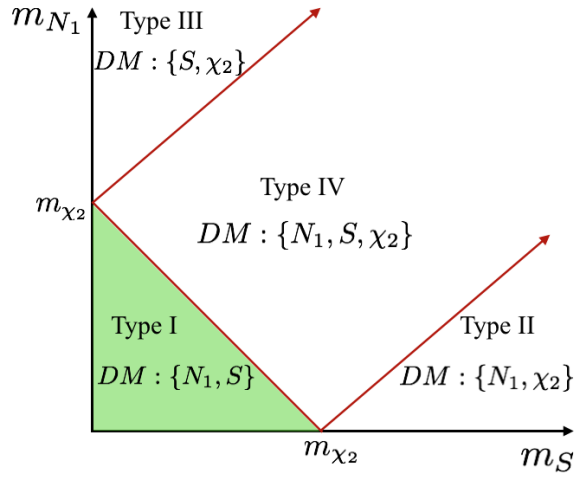


Figure 2: Different types of multicomponent DM scenarios that can be realised in the model depicted in $m_{N_1} - m_S$ plane, given that a hierarchy among m_{N_1}, m_S, m_{χ_2} . Type-I scenario (coloured in green) is analysed in this paper.

- Type-I : $m_{\chi_2} > m_{N_1} + m_S$: N_1 and S are the stable DM components.
- Type-II: $m_S > m_{N_1} + m_{\chi_2}$: N_1 and χ_2 are stable DM components.
- Type-III: $m_{N_1} > m_S + m_{\chi_2}$: S and χ_2 are stable DM components.
- Type-IV: If $m_{\chi_2} < m_{N_1} + m_S$, $m_S < m_{N_1} + m_{\chi_2}$ and $m_{N_1} < m_S + m_{\chi_2}$, then all three particles N_1 , χ_2 and S are stable and will yield a three-component DM scenario.

In this paper, we focus mostly on Type-I scenario (green region in Fig. 2). This gives us an opportunity to compare with the single component cases of the corresponding DM components (N_1 and S), which are very well studied, and indicate the effects of DM-DM conversion employed in this set-up.

3 Review of single component DM frameworks with N_1 and S

Before we discuss the two component DM set up (of Type-I) as advocated above, we need to know the fate of the individual DMs in single component frameworks. We review relic density and direct search allowed parameter space for both vectorlike fermion DM (N_1) and singlet scalar DM (S) in the next two consecutive subsections.

3.1 Single component fermion DM (N_1)

The presence of vector-like fermion singlet (χ_1) and a doublet (N) can give rise to a fermion DM [34], where both transform under a \mathcal{Z}_2 symmetry. The relevant Lagrangian is still given by \mathcal{L}^{VF} as in Eq. 2.3. As described above, the singlet and the neutral component of the doublet mix after EWSB, and the lightest component of the neutral physical states N_1 becomes a stable single component DM.

We note here that the freeze-out abundance of N_1 DM is controlled by the annihilation and co-annihilation channels as detailed in Appendix A (Fig. 23, 24 and 25). Therefore, the important parameters which decide the relic abundance of N_1 are

$$\{m_{N_1}, \Delta m, \sin \theta\}.$$

Due to singlet-doublet mixing, the DM in direct search experiments can scatter off the target nucleus via both Z and Higgs mediated processes (shown in top panel of Fig. 9).

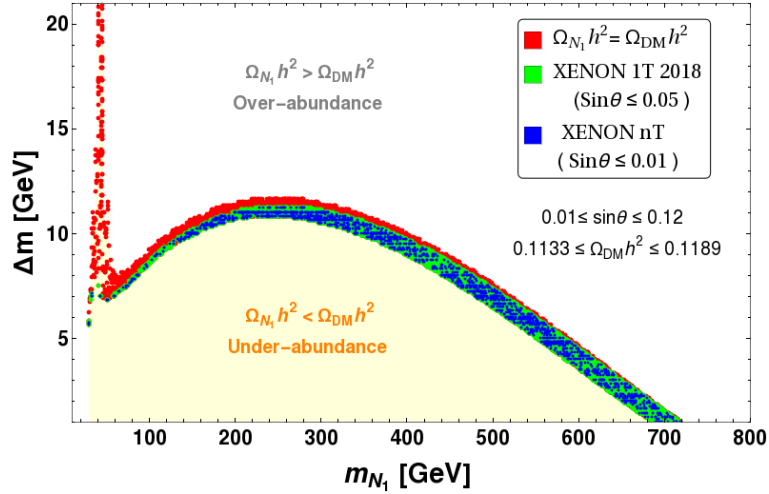


Figure 3: Relic density allowed (red points) and direct detection {XENON 1T (green points), XENON nT (blue points)} allowed parameter space for single component fermion DM (N_1) is shown in $m_{N_1} - \Delta m$ plane. Under abundance ($\Omega_{N_1} h^2 < \Omega_{DM} h^2$) (yellow region below the red points) and over-abundance ($\Omega_{N_1} h^2 > \Omega_{DM} h^2$) (the region above the red points) are also indicated. $\Omega_{DM} h^2$ range is mentioned in the figure inset and also in Eqn. 2.19.

The relic density and direct search allowed parameter space for N_1 DM is shown in Fig. 3. This is shown in $m_{N_1} - \Delta m$ plane for small values of $\sin \theta$. It has already been

noted [34] that due to Z mediation, $\sin\theta$ is limited to very small values $\lesssim 0.1$ by the non-observation of DM in direct search experiments. We therefore choose only such small mixing regions for illustration in Fig. 3. Essentially, the whole relic density allowed plane is also allowed by direct search constraints (XENON1T [10], XENON nT [11] as shown in the Fig. 3). The under and over abundant regions are also indicated, which will be more useful for discussing the two component framework. The important message from this graph is that for small $\sin\theta$, Δm has to be small ($\lesssim 12$ GeV) to satisfy relic density, except for those low DM mass resonance regions ($\sim m_Z/2$, $m_h/2$). For under abundance, the DM has to obtain even higher annihilation cross-section. For small $\sin\theta$ to satisfy direct search, the only way to probe under abundant regions is to have even smaller Δm to enhance co-annihilation effects. Therefore, when we embed the fermion DM in a non-interacting two component DM framework, the under abundant regions (as indicated in Fig. 3) are going to be allowed. However, the situation alters in presence of an interacting two-component framework as we will demonstrate in Section 4.

3.2 Single component scalar DM (S)

The Lagrangian \mathcal{L}^{Scalar} in Eqn. 2.4, describes the case of single component scalar DM S . The relevant parameters describing the scalar DM interaction with SM is given by

$$\{m_S, \lambda_{SH}\}.$$

The annihilation process which controls the freeze-out of S are shown in Fig. 4.

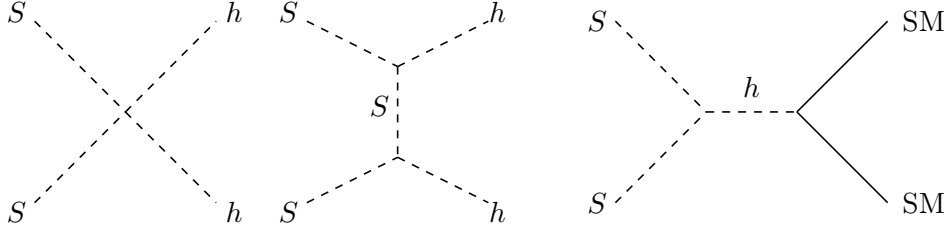


Figure 4: Feynman diagrams for Scalar DM S annihilating to SM particles i.e $S S \rightarrow$ SM SM.

The relic density allowed parameter space for the scalar DM is well studied [20, 21, 32, 33, 37] and is summarised in Fig. 5, in terms of DM mass (m_S) and Higgs portal coupling (λ_{SH}). Direct search sensitivities of LUX [9] and XENON 1T [10] from null detection are also shown in the same graph for S which only has a t -channel Higgs mediation with nucleus (shown in bottom pannel of Fig. 9). This essentially shows that if S contributes to the full DM relic density, it lives either in resonance region ($m_S \sim m_h/2$) or in high DM mass regions ($m_S \gtrsim 900$ GeV) to satisfy null observations from direct search experiments. Under abundance for S can only be achieved with larger annihilation cross-section, that can only occur with larger Higgs portal coupling (λ_{SH}) and that is even more constrained from direct search data. If the scalar DM is embedded in an non-interacting multi-component DM

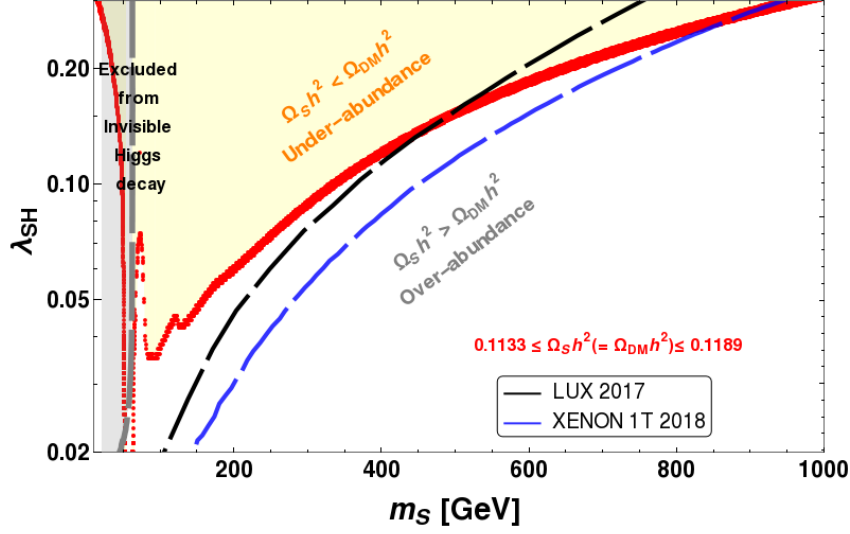


Figure 5: Relic density allowed ($\Omega_S h^2 = \Omega_{DM} h^2$) (red region) parameter space for scalar DM (S) is shown in $m_S - \lambda_{SH}$ plane. LUX [9] (black dashed) and XENON 1T [10] (blue dashed) exclusion limits are also shown. The region ‘above’ the red patch (in yellow) corresponds to under abundance ($\Omega_S h^2 < \Omega_{DM} h^2$) and the one below corresponds to over abundance ($\Omega_S h^2 > \Omega_{DM} h^2$). Exclusion limit from invisible Higgs decays is shown by grey region. $\Omega_{DM} h^2$ range is mentioned in the figure inset and also in Eqn. 2.19.

framework, it is further restricted by direct search, discarding m_S upto TeV or more. We will show in Section 4, that the situation alters in presence of an additional DM component, with which the scalar DM has non-negligible interactions. We also point out that the presence of a heavy scalar S_H (also a SM singlet) having same \mathcal{Z}_2 charge as of S , can change the conclusion significantly allowing a larger parameter space through co-annihilation (in Section 5).

4 Two Component DM with N_1 and S

As already discussed in Section 2.2, we choose Type-I case for illustrating a two-component interacting DM model with $m_{\chi_2} > m_{N_1} + m_S$, where N_1 forms a vectorlike fermion DM component and S forms a scalar DM component. The heaviest field χ_2 in the dark sector, which can decay to N_1 and S , act as a mediator between the two DM components through the Yukawa interaction: $Y_2 \bar{\chi}_2 \chi_1 S$. These DMs can also interact with each other through Higgs portal couplings: $Y_1 \bar{N} \tilde{H} \chi_1$ and $\lambda_{SH} (H^\dagger H) S^2$. The DM-DM interactions of this model is shown by the Feynman diagrams in Fig. 6.

DM-DM conversion diagrams will dominantly help the heavier DM component to annihilate into the lighter one and therefore contribute to its thermal freeze-out and relic density. Apart from DM masses and mediator mass (m_{χ_2}), the DM-DM conversion is a function of the following couplings

$$\{Y_1, Y_2, \lambda_{SH}\}.$$

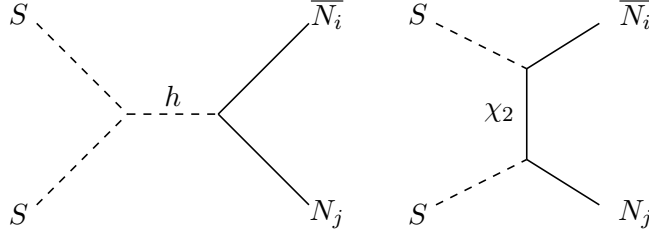


Figure 6: Diagrams contributing to DM-DM conversion ($i = 1, 2$) between fermion (N_i) and scalar DM (S) components.

However, the Higgs portal couplings Y_1 (as a function of Δm and $\sin \theta$, see in Eqn. 2.10) and λ_{SH} are strongly constrained from direct detection bound (already discussed in section 3). Therefore, DM-DM interaction through Higgs mediation will be negligible in relic density and direct search allowed parameter space of the two component model and can be identified with $Y_2 = 0$ situation. We will show that in such a case, the two DMs are almost decoupled and behave like single component cases to occupy the under abundant regions of their corresponding DM parameter space. Here lies the importance of assuming the presence of a heavy mediator χ_2 in this model to carry out DM-DM interactions through Yukawa coupling Y_2 .

4.1 Coupled Boltzmann Equations

The thermal freeze-out of two component DM framework is described by a coupled Boltzmann equations (BEQs) and can be written as a function of reduced x , where $x = \mu/T$, with $\frac{1}{\mu} = \frac{1}{m_{N_1}} + \frac{1}{m_{N_2}} + \frac{1}{m_S}$ [20, 25, 43]. The one here reads:

$$\begin{aligned}
\frac{dY_{N_i}}{dx} = & -0.264 M_{Pl} \sqrt{g_*} \frac{\mu}{x^2} \left[\sum_j \left\{ \langle \sigma v_{\overline{N_i} N_j \rightarrow SM} \rangle (Y_{N_i} Y_{N_j} - Y_{N_i}^{EQ} Y_{N_j}^{EQ}) \right. \right. \\
& + \langle \sigma v_{\overline{N_i} N_j \rightarrow SS} \rangle \left(Y_{N_i} Y_{N_j} - \frac{Y_{N_i}^{EQ} Y_{N_j}^{EQ}}{Y_S^{EQ^2}} Y_S^2 \right) \Theta(m_{N_i} + m_{N_j} - 2m_S) \\
& - \langle \sigma v_{SS \rightarrow \overline{N_i} N_j} \rangle \left(Y_S^2 - \frac{Y_S^{EQ^2}}{Y_{N_i}^{EQ} Y_{N_j}^{EQ}} Y_{N_i} Y_{N_j} \right) \Theta(2m_S - m_{N_i} - m_{N_j}) \Big\} \\
& + \langle \sigma v_{\overline{N_i} N^\pm \rightarrow SM} \rangle (Y_{N_i} Y_{N^\pm} - Y_{N_i}^{EQ} Y_{N^\pm}^{EQ}) \Big], \\
\frac{dY_S}{dx} = & -0.264 M_{Pl} \sqrt{g_*} \frac{\mu}{x^2} \left[\langle \sigma v_{SS \rightarrow SM} \rangle (Y_S^2 - Y_S^{EQ^2}) \right. \\
& + \sum_{i,j} \left\{ - \langle \sigma v_{\overline{N_i} N_j \rightarrow SS} \rangle \left(Y_{N_i} Y_{N_j} - \frac{Y_{N_i}^{EQ} Y_{N_j}^{EQ}}{Y_S^{EQ^2}} Y_S^2 \right) \Theta(m_{N_i} + m_{N_j} - 2m_S) \right. \\
& + \langle \sigma v_{SS \rightarrow \overline{N_i} N_j} \rangle \left(Y_S^2 - \frac{Y_S^{EQ^2}}{Y_{N_i}^{EQ} Y_{N_j}^{EQ}} Y_{N_i} Y_{N_j} \right) \Theta(2m_S - m_{N_i} - m_{N_j}) \Big\} \Big],
\end{aligned}$$

$$(4.1)$$

where the subscripts $i, j = 1, 2$ describes the fermion DM and the heavy neutral fermion component of the model respectively. In the above equations, we note that the annihilation contribution of N_i to S or otherwise depending on the mass hierarchy is included. The equilibrium distributions now recast in terms of μ takes the form:

$$\begin{aligned} Y_{N_i}^{EQ}(x) &= 0.145 \frac{g}{g_*} x^{\frac{3}{2}} \left(\frac{m_i}{\mu} \right)^{\frac{3}{2}} e^{-x \left(\frac{m_i}{\mu} \right)} \\ Y_S^{EQ}(x) &= 0.145 \frac{g}{g_*} x^{\frac{3}{2}} \left(\frac{m_S}{\mu} \right)^{\frac{3}{2}} e^{-x \left(\frac{m_S}{\mu} \right)} \end{aligned} \quad (4.2)$$

The relic density allowed parameter space of the two-component framework is then given by the solution of the above Boltzmann equations, that determine the freeze-out of the individual components depending on annihilations plus co-annihilations and DM-DM interactions. Obviously, total DM relic density for the two component case will be the sum of individual relic density as:

$$\Omega_T h^2 = \Omega_{N_1} h^2 + \Omega_S h^2, \quad (4.3)$$

which should satisfy combined WMAP and PLANCK limit $0.1133 \leq \Omega_T h^2 (= \Omega_{DM} h^2) \leq 0.1189$ [6]. Individual relic density in interacting multipartite DM case can be found out by numerical solution to the coupled Boltzmann equations or approximate analytical solution of coupled BEQ [20] and that of the i -th DM candidate is given by:

$$\Omega_i h^2 = \frac{854.45 \times 10^{-13}}{\sqrt{g_*}} \frac{x_f^i}{\langle \sigma v \rangle_i^T}, \quad (4.4)$$

where $\langle \sigma v \rangle_i^T$ is the total effective annihilation cross-section and x_f^i corresponds to freeze-out temperature of the i th DM component. Note however, for the ease of the analysis, we are not using the approximate solution here; relic density and direct search cross-sections for both the DM components are obtained numerically by inserting the model in **MicrOmegas** package [44].

If fermion DM is heavier than scalar DM ($m_{N_1} > m_S$), then heavier DM component (N_1) can annihilate to lighter component (S) following processes as in Fig. 6. Such DM-DM conversion affects the freeze out of heavier DM component and hence its relic density [20]. The lighter DM candidate on the other hand, have no new channel to deplete its number density and behave almost like single component DM. Then $\langle \sigma v \rangle_{N_1}^T$ for fermionic DM assuming $m_{N_1} > m_S$ will be given by:

$$\langle \sigma v \rangle_{N_1}^T \simeq \langle \sigma v \rangle_{N_1}^{eff} + \langle \sigma v \rangle_{\bar{N}_1 N_1 \rightarrow SS} + 2 \langle \sigma v \rangle_{\bar{N}_1 N_2 \rightarrow SS} \left(1 + \frac{\Delta m}{m_{N_1}} \right)^{3/2} e^{\frac{-\Delta m}{T}}, \quad (4.5)$$

where $\langle \sigma v \rangle_{N_1}^{eff}$ is the annihilation plus co-annihilation cross-section of fermion DM to SM given by Eq. A.1. The last term in the above equation represents co-annihilation to scalar DM component and is therefore aided by the Boltzmann factor along with a symmetry

factor of 2 (assuming $m_{N_1} \simeq m_{N_2}$). In this limit of $m_{N_1} > m_S$, the annihilation cross-section for scalar DM (S) only captures the annihilations to SM as in a single component framework:

$$\langle\sigma v\rangle_S^T = \langle\sigma v\rangle_{SS\rightarrow SM\ SM} . \quad (4.6)$$

Evidently, for the opposite hierarchy, $m_S > m_{N_1}$:

$$\begin{aligned} \langle\sigma v\rangle_{N_1}^T &= \langle\sigma v\rangle_{N_1}^{eff}, \\ \langle\sigma v\rangle_S^T &= \langle\sigma v\rangle_{SS\rightarrow SMSM} + \langle\sigma v\rangle_{SS\rightarrow \overline{N_i}N_j}. \end{aligned} \quad (4.7)$$

We note here that the relic density of the lighter DM may also get affected by DM-DM conversion when the production from the heavier component becomes significantly large and comparable to its annihilation to SM. This is to remind again that the parameter space scan performed in the subsequent analysis do not use approximate solutions to the coupled BEQs derived above but uses the numerical results obtained from the code `MicrOmegas` which nicely captures all the features of individual DM relic density affected by DM-DM conversion.

4.2 Relic density and direct search outcome

We first study the variation of individual relic densities with corresponding DM masses as shown in Fig. 7. Two possible mass hierarchies are shown; in top we choose $m_S > m_{N_1}$ and in the bottom panel we have $m_S < m_{N_1}$. Relic density of fermion DM (N_1) is shown in the left panel and that of the scalar (S) is shown in the right panel. We see that for $m_S > m_{N_1}$ (top left panel of Fig. 7), $\Omega_{N_1}h^2$ do not change with different choices of Yukawa coupling Y_2 . However with same hierarchy ($m_S > m_{N_1}$) for S , relic density is steadily reduced with larger choice of Y_2 (top right panel). It is exactly the other way round, when we have $m_S < m_{N_1}$ (bottom panel of Fig. 7). In such a case, relic density for N_1 decreases with larger Y_2 , while it remains unaltered for S . This follows from the analytic solution of the effective annihilation cross sections as mentioned in Eqs. 4.5, 4.6, 4.7 showing the importance of DM-DM conversion. In this plot we have kept other parameters fixed as mentioned in the plot, particularly with a moderate value of the mediator mass fixed at $m_{\chi_2} = 500$ GeV.

The sensitivity of individual relic densities to DM-DM conversion as a function of mediator mass (m_{χ_2}) is shown in Fig. 8. Evidently, we demonstrate it for the heavier component (N_1 on the left and S on the right) with different choices of mediator masses: m_{χ_2} : 500 (red), 1000 (green) and 2000 (blue) GeV, keeping $Y_2 = 1.0$ and $\lambda_{SH} = 0.1$ fixed. In the same Fig. 8, we have also demonstrated the case of $Y_2 = 0$ (purple dotted line), when χ_2 does not take part in the DM-DM conversions. It is evident that with large m_{χ_2} , DM-DM conversion becomes feeble and closely resembles $Y_2 = 0$ (purple dotted line) case. Therefore, large Yukawa Y_2 can play an important role in relic density, but with not-so-heavy mediator mass (m_{χ_2}). The lighter DM component is again mostly unaffected by DM-DM conversion as has already been discussed. One important point to note is the difference between $Y_2 = 1.0$ and $\lambda_{SH} = 0.1$ chosen for illustration. This is because Y_2

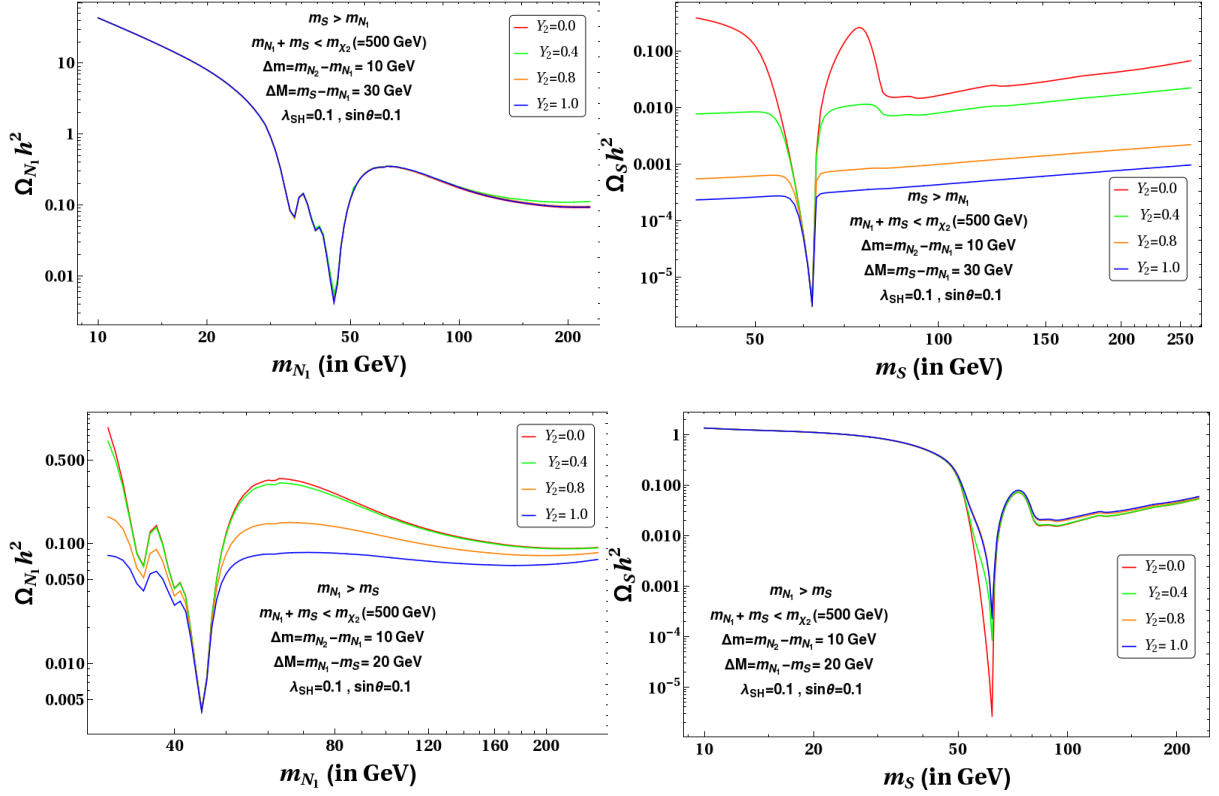


Figure 7: Relic densities ($\Omega_{N_1} h^2$ and $\Omega_S h^2$) of the individual DM components as a function of respective DM masses (m_{N_1} and m_S) shown in left and right panel respectively. Two possible mass hierarchies are shown: $m_S > m_{N_1}$ (top panel) and $m_{N_1} > m_S$ (bottom panel). Different values of $Y_2 = 0.0$ (red) , 0.4 (green) , 0.8 (orange) , 1.0 (blue) are chosen keeping other parameters fixed (as mentioned in the plots) to decipher DM-DM interactions.

remains unconstrained (excepting for large perturbative limit $\leq \sqrt{4\pi}$), while λ_{SH} is highly restricted by direct search (recall Fig. 5). We can also see that $m_{\chi_2} = 2 \text{ TeV}$ closely mimic $Y_2 = 0$ case for fermion DM, while it does not completely do so for Ω_S . This is because of very small annihilation cross-section of the scalar DM to SM compared to DM-DM conversion due to the choice of small λ_{SH} .

Let us now turn to direct search constraints of this two component DM set up. Feynman graphs for direct search contribution of the DM components are shown in Fig. 9. Fermion DM (N_1) has both Z and Higgs mediated interaction, while the scalar (S) interacts only through Higgs mediation. Direct search cross-sections for individual components are well known; however in two-component set up, the direct search cross-section for each component

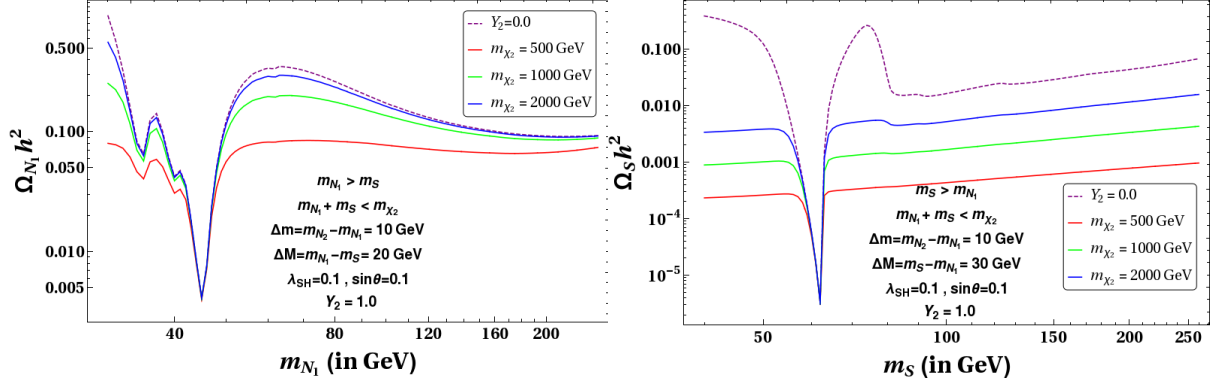


Figure 8: Sensitivity of mediator mass (m_{χ_2}) to DM-DM conversion and that to relic density of the heavier component is demonstrated. [Left] $\Omega_{N_1} h^2$ as a function of m_{N_1} for different values of $m_{\chi_2} = 500$ (red) , 1000 (green) , 2000 GeV (blue) assuming $m_{N_1} > m_S$. [Right] $\Omega_S h^2$ as a function of m_S for $m_S > m_{N_1}$. Other parameters kept fixed at different values are mentioned in the plot along with $Y_2 = 1.0$ and $\lambda_{SH} = 0.1$. Purple dotted line in both graphs correspond to $Y_2 = 0$ case, shown for comparison.

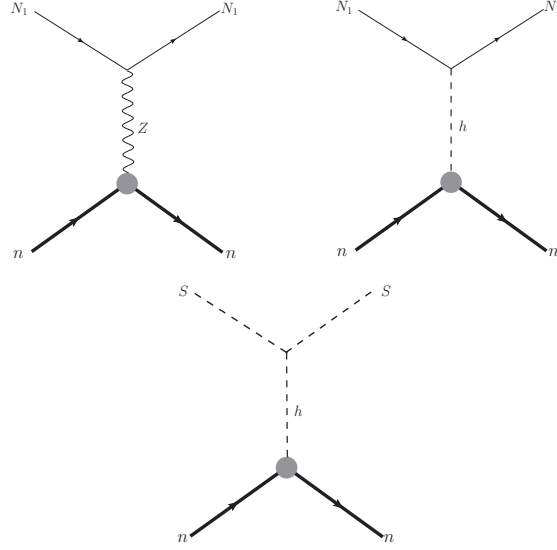


Figure 9: Feynman diagrams of spin independent (SI) direct detection of fermion DM (top panel) and scalar DM (bottom panel).

is folded by their fraction of relic density as²:

$$\sigma_{eff}^{SI}(S) = \left(\frac{\Omega_S h^2}{\Omega_T h^2} \right) \sigma_S^{SI}, \quad (4.8)$$

²The actual limit from direct search on multipartite DM scenarios need to account for mass sensitivity on the nuclear recoil, the details can be found here [20, 25].

and

$$\sigma_{eff}^{SI}(N_1) = \left(\frac{\Omega_{N_1} h^2}{\Omega_T h^2} \right) \sigma_{N_1}^{SI}. \quad (4.9)$$

Spin independent direct search cross-sections for both DM components (σ_S^{SI} and $\sigma_{N_1}^{SI}$) are obtained from inserting the model into the code `MicrOmegas` [44]. No signal for DM in direct search experiments like LUX [9], XENON 1T [10] so far put a strong constraint on the WIMP-like DM scenarios as we have here. Recall that scalar DM lives only in the high mass region (≥ 900 GeV) except for resonance ($\sim m_h/2$) and fermion DM lives in $\sin \theta \leq 0.1$ region with a small Δm in their single component set up. The question is how much the above conclusions get relaxed in a two component set up with large DM-DM conversion as adopted here.

Case I: Feeble DM-DM interactions with $Y_2 = 0$

Let us now turn to relic density ($0.1133 \leq \Omega_T h^2 \leq 0.1189$) and SI direct search allowed parameter space of this two component model. We will first study the case for negligible DM-DM interactions with $Y_2 = 0$. The results are summarised in Fig. 10. We show the relic density allowed parameter space in upper panel, in the left for N_1 and in the right for S . With $Y_2 = 0$, the two DM-components behave as if they are decoupled and the allowed parameter space only opens up in the under-abundant regions of those individual DMs (compare the single component cases as demonstrated before in Fig. 3 and Fig. 5). Different colour codes indicate the percentage of the individual DM density as indicated in the figure inset. It is understood that given a certain percentage of one DM, rest of DM relic density is composed of the other component. So any combination is essentially possible by relic density constraint. In the bottom panel of Fig. 10, we show the allowed parameter space after direct search constraints from PANDA where both DMs simultaneously satisfy direct search bound from PANDA [12]. Note here that there are no parameter space where effective DD cross-section (in Eqs. 4.8, 4.9) of both N_1 and S DM simultaneously goes beyond recent XENON-1T limit [11]. For fermion DM, direct search allowed parameter space spans the whole of under-abundant parameter space as it doesn't constrain the small Δm region further with small singlet-doublet mixing $\sin \theta \leq 0.05$, as we have chosen for the scan. We have already explained that for fermion DM, direct search crucially controls $\sin \theta$ only, which is well below the required cut-off. On the other hand, scalar DM is severely constrained by direct search constraint in $m_S - \lambda_{SH}$ plane, which leaves Higgs resonance (not shown in the plot) and heavy Scalar DM mass region ($m_S \geq 900$ GeV) only. In the heavy scalar mass region, the relic density is $\gtrsim 80\%$, therefore allowing only a tiny fraction of fermion DM. The whole analysis at $Y_2 = 0$ also shows that the presence of s -channel Higgs mediated DM-DM interactions to be very feeble to alter the freeze-out of any of the DM component as mentioned earlier.

Case II: The case of DM-DM interactions with $Y_2 \neq 0$

In Fig. 11, we show the relic density and direct search allowed parameter space of the model with a non-zero Yukawa coupling ($Y_2 \neq 0$, $0.1 \leq Y_2 \leq 1.6$). Relic density allowed

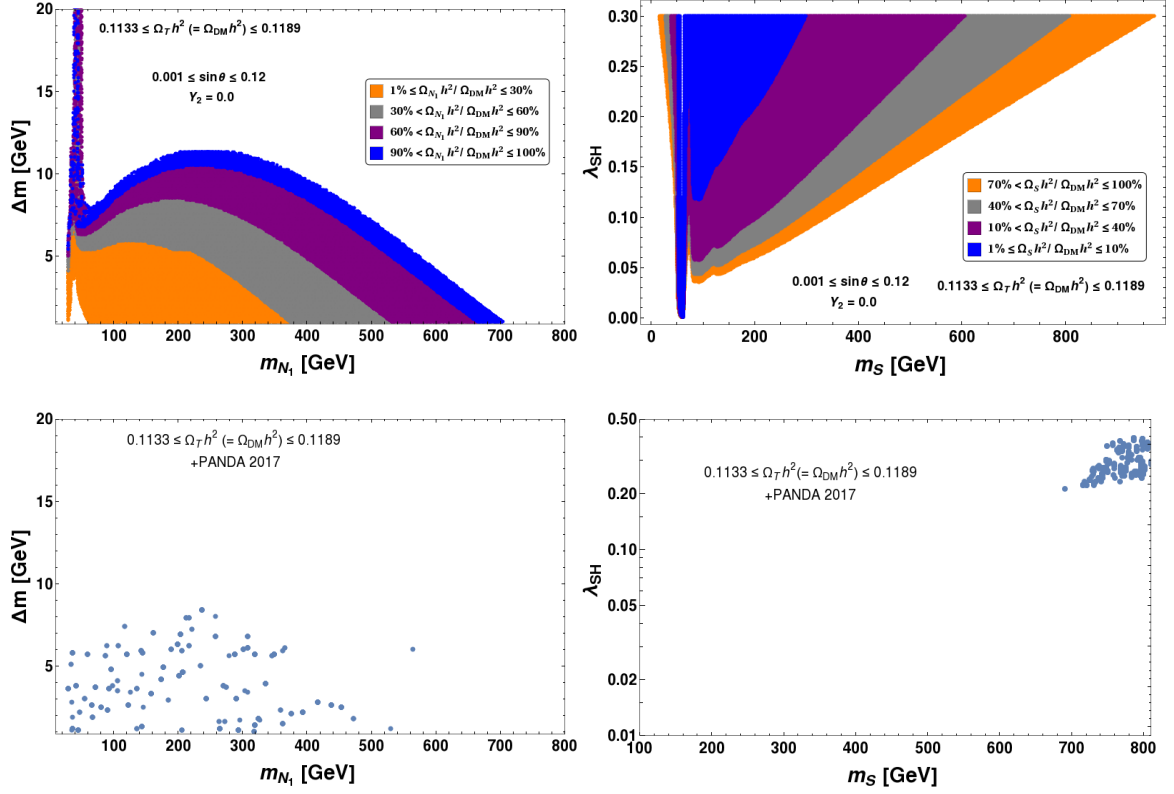


Figure 10: [Top Panel] Relic density allowed regions of two component DM scenario $\{N_1, S\}$ in $m_{N_1} - \Delta m$ (top left) and $m_S - \lambda_{SH}$ (top right) for $Y_2 = 0$. Different colour codes indicate the fraction of individual relic density $\frac{\Omega_i}{\Omega_T}$ varied in different ranges as mentioned in inset. [Bottom Panel] Relic density and direct detection (PANDA 2017 [12]) allowed parameter space in $m_{N_1} - \Delta m$ (bottom left) and $m_S - \lambda_{SH}$ (bottom right) planes.

parameter space is shown in the upper panel for N_1 (in $m_{N_1} - \Delta m$ plane) on left and for S (in $m_S - \lambda_{SH}$ plane) on right. Both possible mass hierarchies are studied and depicted; (i) $m_{N_1} > m_S$ by orange and (ii) $m_S > m_{N_1}$ by blue points. We see that when $m_S > m_{N_1}$, the whole $m_S - \lambda_{SH}$ parameter space is allowed (blue points in top right plot), where smaller λ_{SH} is substituted by larger Y_2 appropriately. On the other hand, N_1 DM has the fate of single component DM with under abundance adjusted to the other component when $m_S > m_{N_1}$ (blue points in top left plot). This is exactly the other way round, when we choose $m_S < m_{N_1}$; the whole $m_{N_1} - \Delta m$ plane becomes allowed (orange points in top left plot) and S has the fate of single component DM filling the under abundance region (orange points in top right plot). This is possible because of DM-DM conversion that we introduced in this model through the heavy mediator χ_2 with Y_2 Yukawa interaction. With $m_{N_1} > m_S$, the effective annihilation required for fermion DM to acquire required relic density ($\Omega_{N_1} h^2 < \Omega_{DM} h^2$) in small $\sin \theta$ region no longer depends on small Δm through co-annihilation because of additional annihilation channel to scalar DM. We will focus on

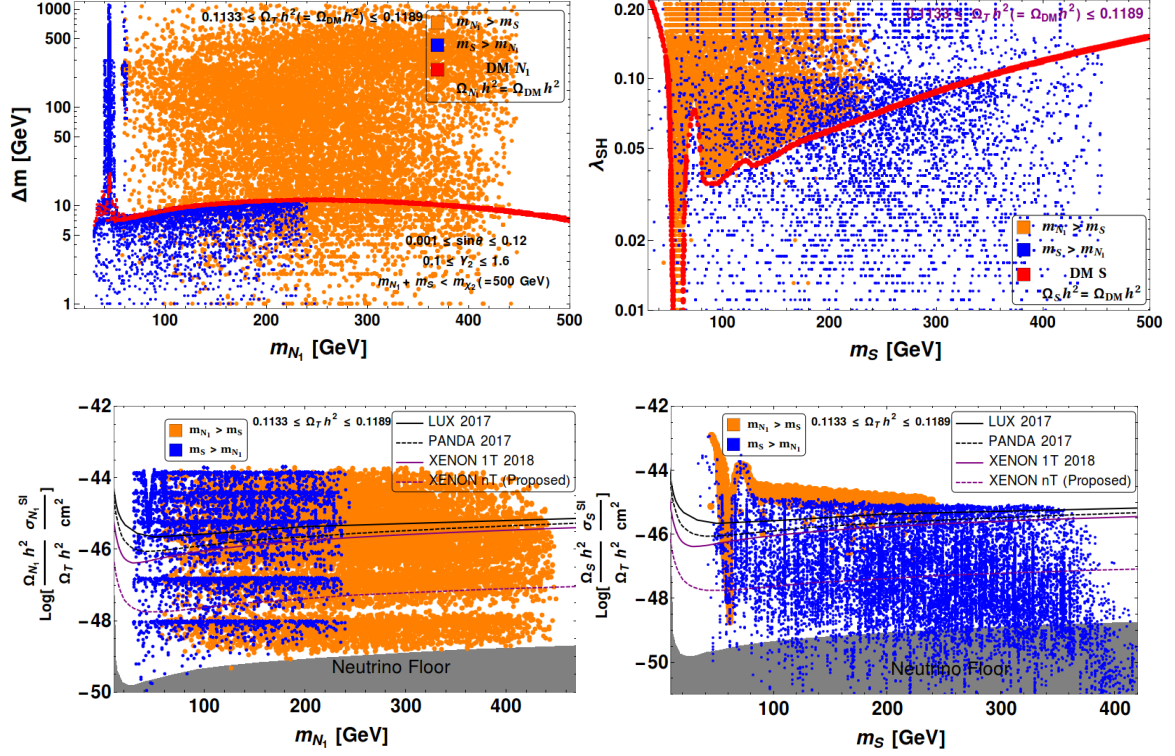


Figure 11: [Top Panel] Relic density allowed parameter space for two component DM model in $m_{N_1} - \Delta m$ (top left) and $m_S - \lambda_{SH}$ (top right) planes. Two mass hierarchies : $m_{N_1} > m_S$ (orange points) and $m_S > m_{N_1}$ (blue points) are shown in both plots. Red points depict the case of single component DM scenarios, for N_1 on the left and for S on the right panel. [Bottom Panel] Relic density allowed points are shown in DM mass vs effective SI DM-nucleon cross-section planes; $\left(\frac{\Omega_{N_1} h^2}{\Omega_T h^2}\right) \sigma_{N_1}^{SI} - m_{N_1}$ in bottom left and $\left(\frac{\Omega_S h^2}{\Omega_T h^2}\right) \sigma_S^{SI} - m_S$ in bottom right. Limits from different DD experiments, LUX [9](black solid line), recent PANDA [12] (black dashed), XENON 1T [10] (purple solid line) and predicted XENON nT [11] (purple dotted line) are also indicated in the figures. Shaded region correspond to Neutrino floor where DM signal cannot be distinguish from neutrino background.

this particular case for collider signatures of this model at the LHC. In the bottom panel of Fig. 11, we show the effective SI direct search cross-section for both DM components at relic density allowed points ($\Omega_i h^2 < \Omega_{DM} h^2$) for both the mass hierarchies. The limits from LUX [9], PANDA [12], XENON 1T [10] and XENON nT [11] are shown. The plots in the bottom panel point out to a larger available parameter space for the heavier DM component. This is simply due to freeze-out of the heavier component being governed by DM-DM conversion, not affecting direct search significantly. The scans in Fig. 11 are limited to DM mass within $\lesssim 500$ GeV as it has been done for a mediator mass $m_{\chi_2} = 500$ GeV to satisfy $m_{N_1} + m_S < m_{\chi_2}$.

The outcome of relic density and direct search (XENON 1T limits [10] from the bottom

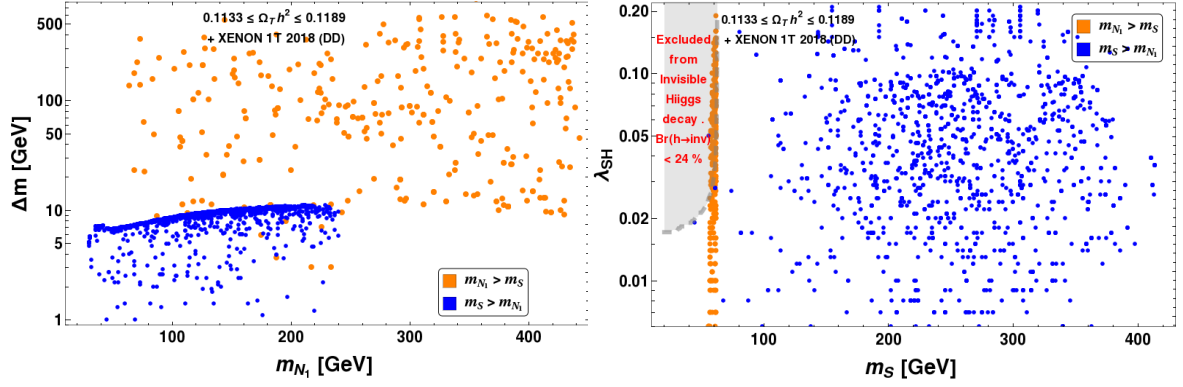


Figure 12: Relic density and direct search (XENON 1T data [10]) allowed parameter space is shown for both N_1 and S components in $m_{N_1} - \Delta m$ (left) and $m_S - \lambda_{SH}$ (right) plane. Two possible mass hierarchies: $m_{N_1} > m_S$ (orange points) and $m_S > m_{N_1}$ (blue points) are indicated in both planes. Invisible Higgs branching constraint is also shown in the right panel which discards a significant part of $m_S < m_h/2$ region.

panel of Fig. 11) constraints put together yield Fig. 12. The constraints on fermion DM in $m_{N_1} - \Delta m$ plane (left) is obviously less restrictive as we choose small $\sin \theta \lesssim 0.05$ for the scan, thus allowing the whole parameter space with upto $\Delta m \gtrsim 500$ or more for $m_{N_1} > m_S$ (orange points in left plot) thanks to conversion to the scalar DM. This feature serves as the most interesting phenomenological outcome of this model, as we discuss in collider section. For $m_{N_1} > m_S$, the scalar DM however is allowed only in the resonance region ($m_S \sim m_h/2$) as can be seen by orange points in the right plot of Fig. 12. This is already expected as direct search tames down the relic density allowed scalar DM parameter space absent DM-DM conversion. For the reverse hierarchy $m_{N_1} < m_S$ (blue points), fermion DM is allowed only in the under-abundant regions of its single component manifestation, whereas it allows a larger mass range of scalar DM, thanks again to the possible DM-DM conversion with a lighter N_1 . Invisible Higgs branching ratio $Br(h \rightarrow \text{inv}) < 0.24$ [42], puts a significant constraint for the scalar DM with $m_S < m_h/2$. But for fermion DM, this doesn't discard any parameter space given the small values of $\sin \theta$ chosen for the scan.

A possible mass correlation of these two DM components is studied next and depicted in Fig. 13 in $m_{N_1} - m_S$ plane for satisfying relic density and direct search constraints. On the left panel, we show that the whole triangle designated by the kinematic limit $m_{N_1} + m_S < m_{\chi_2}$, with $m_{\chi_2} = 500$ GeV chosen for the scan is allowed by relic density constraint. However direct search (XENON1T data [10]) restricts it significantly for $m_{N_1} > m_S$, allowing only scalar DM to lie in resonance $m_h/2$, while it is not that restrictive for the other hierarchy $m_{N_1} < m_S$, as shown by the spread of blue points filling almost entirely the upper part of the triangle. The thick black line depicting $m_{N_1} = m_S$ separates these two hierarchies. The plot on the right panel shows the allowed points in $m_{N_1} - m_S$ plane to satisfy relic density for different ranges of Δm . It shows that small $1 \leq \Delta m \leq 12$ GeV is allowed

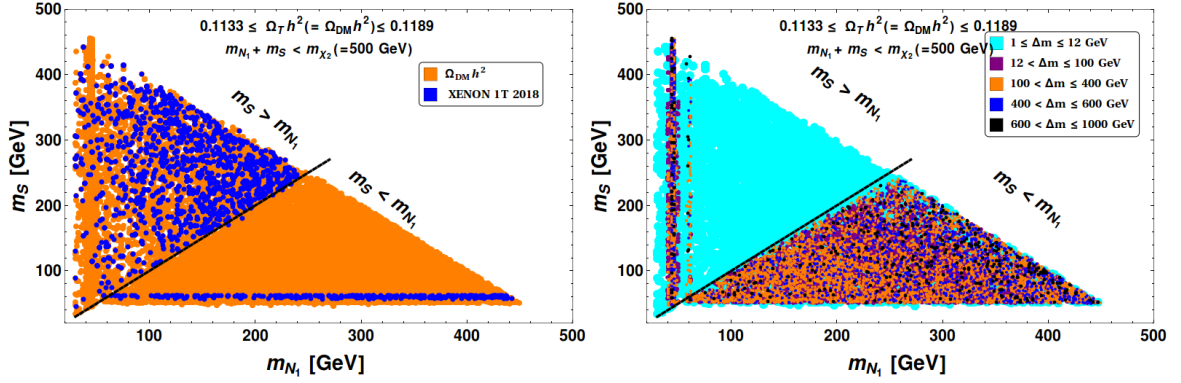


Figure 13: Mass correlation of the two DM components in $m_{N_1} - m_S$ plane. [Left Panel] Relic density allowed parameter space is shown by orange points and direct search constraint from XENON 1T [10] on both N_1 and S is shown by blue points. Black solid line corresponding to $m_{N_1} = m_S$ segregates the two possible hierarchies: the one above corresponds to $m_S > m_{N_1}$ and the region below has $m_S < m_{N_1}$. [Right Panel] Relic density allowed points for different ranges of Δm shown with different colour codes.

throughout the parameter space while large Δm is restricted to $m_{N_1} > m_S$ as we already discussed. For $m_{N_1} < m_S$, one can have larger Δm allowed only in the resonance region $m_{N_1} \sim m_h/2$ and $\sim m_Z/2$.

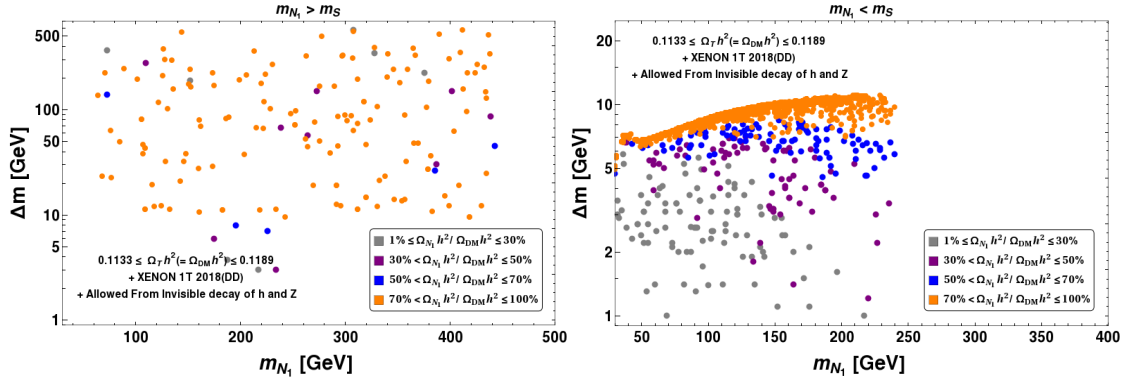


Figure 14: Relic density, direct search (XENON 1T [10]) and invisible decay constrain of Higgs and Z boson [42] allowed parameter space of the two component model (with $Y_2 \neq 0$) in $m_{N_1} - \Delta m$ plane. Percentage of fermion DM component in total relic density within different ranges are shown by different coloured points as detailed in the figure inset. Two different hierarchies $m_S < m_{N_1}$ and $m_S > m_{N_1}$ are shown separately in left and right panel respectively.

Another important question is to know the percentage of fermion or scalar DM com-

ponent present in the allowed parameter space of this two component model. We show the outcome of this exercise in Fig. 14, for fermion DM in $m_{N_1} - \Delta m$ plane. The other component (S) just fills the rest of it and can be gauged from this figure itself. Two possible mass hierarchies $m_S < m_{N_1}$ and $m_S > m_{N_1}$ are shown separately in left and right panel respectively. Fermion DM content in total relic density (for different ranges in percentage) is shown by different colour codes mentioned in the figure inset. All the points also additionally satisfy direct search constraint from XENON1T data [10] and invisible decay constraint of Higgs and Z [42]. The bottom line is that for $m_{N_1} > m_S$, the larger share of DM density is carried by fermion DM with $\Delta m \gg 12$ GeV as it becomes enough to bring the annihilation in the right ballpark through conversion to the scalar DM component (with small $\sin \theta$), while the scalar DM anyway has a large annihilation cross section (and therefore smaller relic density) as it requires to be in the Higgs resonance region ($m_S \sim m_h/2$) to address direct search bound. For the other hierarchy $m_{N_1} < m_S$, under abundant regions of the single component fermion DM is filled up with different percentage as the scalar DM has the freedom to adjust its relic density through its annihilation to SM plus fermion DM.

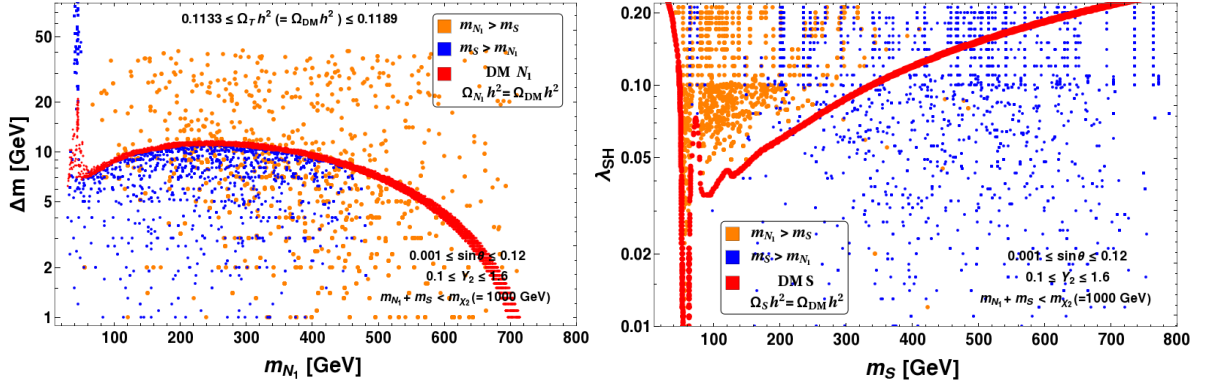


Figure 15: Total relic density allowed regions of two component DM model in $m_{N_1} - \Delta m$ (left panel) and $m_S - \lambda_{SH}$ plane (right panel) with $Y_2 \neq 0$ for mediator mass $m_{\chi_2} = 1000$ GeV. Two mass hierarchies are shown in different colour codes: $m_{N_1} > m_S$ (orange points) and $m_S > m_{N_1}$ (blue points). Red points correspond to the case of single component DM scenarios for N_1 on left and for S on right panel.

So far we have discussed the allowed DM parameters space for the model with a moderate choice of mediator mass, $m_{\chi_2} = 500$ GeV. Now we choose a higher value of χ_2 mass, $m_{\chi_2} = 1000$ GeV to depict relic density allowed limit in $m_{N_1} - \Delta m$ plane (left) and $m_S - \lambda_{SH}$ plane (right) of Fig. 15. Allowed parameter space in $m_{N_1} - \Delta m$ plane becomes more restrictive (Δm spanning roughly upto ~ 50 GeV compared to 500 GeV with $m_{\chi_2} = 500$ GeV) even with $m_{N_1} > m_S$ due to suppressed t-channel DM-DM conversion $\bar{N}_i N_j \rightarrow SS$ due to the heavy mediator (m_{χ_2}). Comparatively, larger parameter space is available for scalar DM S as shown in right panel of Fig. 15 in $m_S - \lambda_{SH}$ plane. This is possible as $SS \rightarrow \bar{N}_i N_j$ with ($Y_2 \neq 0.0$) still dominate over scalar DM annihilation to SM (controlled

BPs	$\{ m_{N_1}, m_S, \lambda_{SH}, Y_2, \sin \theta \}$	Δm	$\Omega_{N_1} h^2$	$\Omega_S h^2$	$\left(\frac{\Omega_{N_1} h^2}{\Omega_{DM} h^2} \right) \sigma_{N_1}^{SI}$ (in cm^2)	$\left(\frac{\Omega_S h^2}{\Omega_{DM} h^2} \right) \sigma_S^{SI}$ (in cm^2)
BPA1	$\{ 79, 256, 0.029, 0.2, 0.02 \}$	6.1	0.0546	0.0641	6.8×10^{-48}	5.9×10^{-47}
BPA2	$\{ 276, 58, 0.010, 0.9, 0.02 \}$	50	0.1092	0.0054	1.5×10^{-48}	1.5×10^{-47}
BPA3	$\{ 131, 61, 0.026, 0.9, 0.01 \}$	101	0.1171	0.0012	1.0×10^{-48}	1.5×10^{-47}
BPA4	$\{ 102, 62, 0.010, 0.9, 0.02 \}$	193	0.1144	0.0010	1.8×10^{-47}	2.0×10^{-48}
BPA5	$\{ 135, 58, 0.004, 1.0, 0.02 \}$	295	0.0840	0.0313	1.5×10^{-47}	1.0×10^{-47}
BPA6	$\{ 127, 62, 0.020, 0.9, 0.01 \}$	377	0.1136	0.0004	1.4×10^{-48}	3.0×10^{-48}
BPA7	$\{ 144, 62, 0.032, 0.9, 0.02 \}$	541	0.1152	0.0002	2.7×10^{-47}	4.2×10^{-48}

Table 2: Some benchmark points allowed by relic density, direct search and invisible Higgs and Z decay limit for mediator mass, $m_{\chi_2} = 500$ GeV. DM masses, couplings, relic density of individual components and effective SI direct search cross-sections are mentioned. All the masses are in GeVs. We mainly focus on $m_{N_1} > m_S$ excepting for BPA1.

by portal coupling λ_{SH}) even with a heavy mediator mass. This feature has already been pointed out while discussing the outcome of DM-DM conversion cross-sections in Fig. 8.

Finally, to summarise the main outcome of the DM analysis is to see that heavier DM component enjoys annihilation to lighter DM for thermal freeze out, relaxing its interaction to visible sector and thus reducing the constraints from direct search cross-sections. Specifically for the two-component case, when scalar DM is heavier than the fermion DM, the Higgs portal coupling can be reduced significantly allowing the scalar DM to be allowed through the entire DM mass plane. On the other hand, when the fermion DM is heavier than the scalar DM, it relaxes the mass difference with the charge companion, allowing larger Δm . No relaxation is possible however for $\sin \theta$ as larger values of mixing is still discarded by Z mediated direct search. The relaxation of Δm plays a crucial role in achieving collider signatures of fermion DM as we illustrate next. We choose a set of benchmark points allowed by relic density and direct search in Table 2 for performing collider analysis, where above features are apparent.

5 Two Component DM in presence of additional heavy scalar

In the two component DM set up, lighter DM component behaves almost as a single component candidate, due to the absence of additional channels for annihilation, thus occupying only under abundant regions accessible from relic density. For $m_{N_1} > m_S$, a large mass splitting Δm can be achieved for a moderated value of mediation mass $m_{\chi_2} \sim 500$ GeV. But at the same time, the scalar DM can only be accommodated at the resonance region, $m_S \approx \frac{m_H}{2}$ (see Fig. 12 and Table 2). This is predictive and restrictive at the same time. This situation however alters significantly if the scalar sector is enlarged with a heavy real scalar S_H which has same charge like S under $\mathcal{Z}_2 \times \mathcal{Z}_2'$ as: $S [-, -]$ and $S_H [-, -]$ [21, 31]. We briefly discuss such a possibility here. The relevant interacting scalar potential is given by:

$$V(S, S_H) \supset \frac{1}{2}m_S^2 S^2 + \frac{1}{2}m_{S_H}^2 S_H^2 + \frac{\lambda_{SH}}{2} \left(H^\dagger H - \frac{v^2}{2} \right) (S^2 + S_H^2) + \lambda_{CH} \left(H^\dagger H - \frac{v^2}{2} \right) S S_H, \quad (5.1)$$

where m_{S_H} is the heavy scalar mass and λ_{CH} is additional (co-annihilation type) Higgs portal coupling. Due to the presence of this interaction, $\lambda_{CH} (H^\dagger H) S S_H$, a new co-annihilation channel, $S S_H \rightarrow SM SM$ opens up. S_H having same charge as of S , is not stable and therefore is not a DM. But the possibility of co-annihilation provides additional channel for scalar DM to freeze out, while it does not contribute to direct search. This is similar to the co-annihilation processes already present in the fermion DM sector. With this, even for $m_{N_1} > m_S$, the scalar DM can be allowed in a large parameter space beyond resonance. Presence of this heavy scalar, also augments dark sector Yukawa interaction providing additional contribution to DM-DM conversion:

$$\mathcal{L}_{\mathcal{DM}}^{Yuk} = -Y_2 (\bar{\chi}_1 \chi_2 S + h.c) - Y_2' (\bar{\chi}_1 \chi_2 S_H + h.c). \quad (5.2)$$

In our numerical analysis, we assume $Y_2 = Y_2'$ for simplicity.

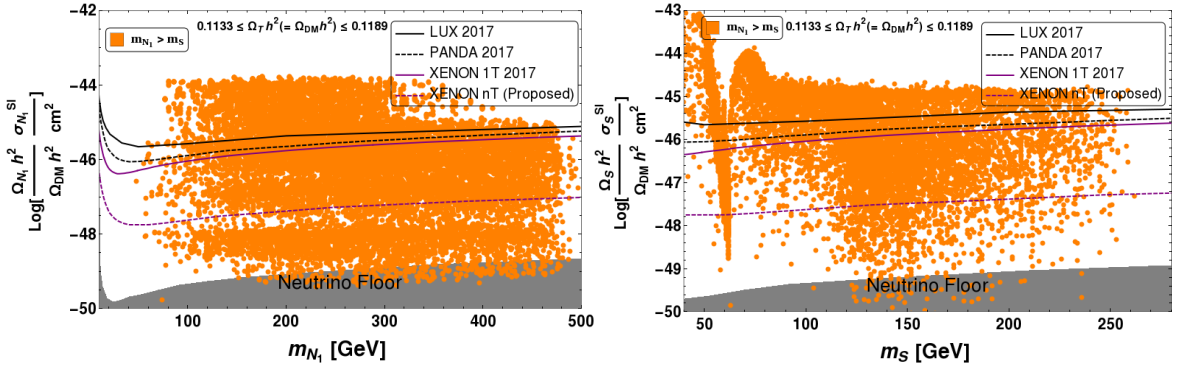


Figure 16: Relic density allowed points plotted in DM mass vs effective SI DM-nucleon cross-section plane: $\left(\frac{\Omega_{N_1} h^2}{\Omega_{DM} h^2} \right) \sigma_{N_1}^{SI} - m_{N_1}$ plane (left) and $\left(\frac{\Omega_S h^2}{\Omega_{DM} h^2} \right) \sigma_S^{SI} - m_S$ plane (right) in presence of heavy scalar S_H . Upper bounds on SI DM-nucleon cross-section from LUX [9] (black solid line), recent PANDA [12] (black dashed), XENON 1T [10] (purple solid line) and predicted XENON nT [11] (purple dotted line) are also indicated in the figures. We have chosen the mass hierarchy: $m_{N_1} > m_S$ and the mediator mass $m_{\chi_2} = 500$ GeV.

The first outcome of this extended two component framework is to show a large parameter space available to the scalar DM through relic density and direct search bounds with the hierarchy $m_{N_1} > m_S$. This is illustrated in Fig. 16. The direct search cross-section for fermion DM in relic density allowed points is shown on the left plot, while that for the scalar is shown in the right panel. We see in the right plot that orange points now span all over the plane with a huge number below the direct search limit unlike being only available in resonance region with the previous case (compare bottom right plot of Fig. 11).

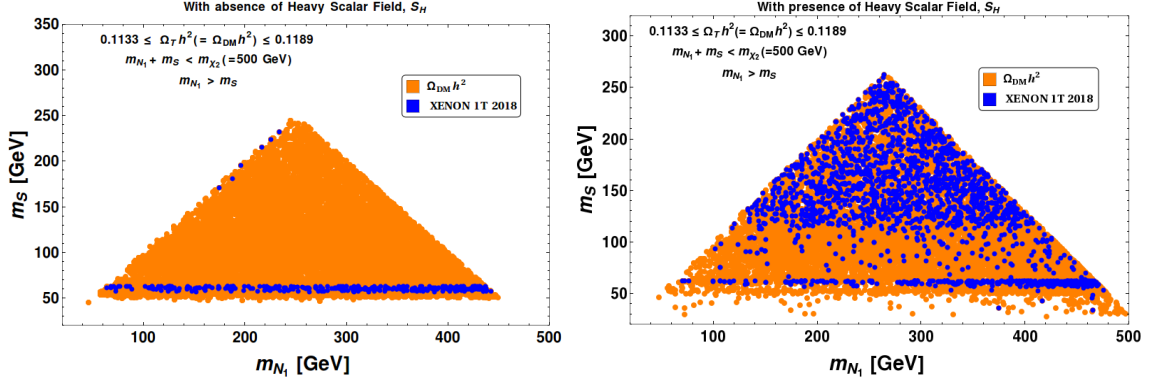


Figure 17: Allowed region of parameters space in $m_{N_1} - m_S$ plane, which satisfy relic density (Orange points) and direct search constraints for both N_1 and S by XENON1T data (blue points) for $m_{N_1} > m_S$. In left panel, we show the original two component scenario in absence of heavy scalar (S_H) and in the right panel, we show it in presence of additional heavy scalar S_H .

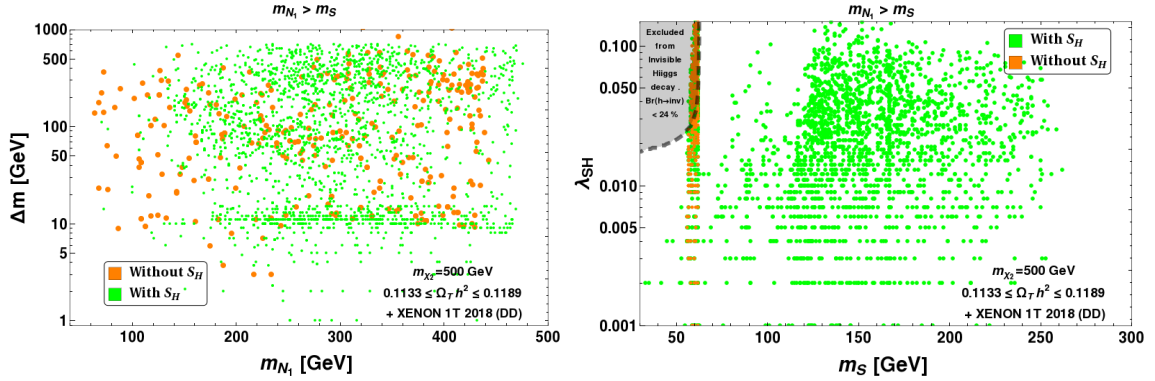


Figure 18: Relic density and direct search (XENON 1T [10]) allowed parameter space of the two component model compared between two cases: (i) original model, in absence of the heavy scalar (S_H) (orange points) and (ii) in presence of a heavy scalar (S_H) (green points) in $m_{N_1} - \Delta m$ plane (left) and $m_S - \lambda_{SH}$ plane (right).

A mass correlation for two DM components is shown in Fig. 17 and compared between the original framework (left) to that in presence of an additional heavy scalar (right). We show that with $m_{N_1} > m_S$, presence of co-annihilation in the scalar sector allows the scalar DM to be present in a larger parameter space after satisfying direct search constraints (plot on the right panel).

Finally, we compare relic density and direct search (XENON 1T [10]) allowed parameter space of the two component model in presence of S_H (green points) to that in absence of S_H (orange points) for both fermion DM and scalar DM components in Fig.18. As expected, we

see that for fermion DM, in $m_{N_1} - \Delta m$ plane (on left panel), there is no difference between these two cases, while for the scalar DM S , the presence of the heavy scalar S_H allows almost all of the plotted parameter space (green points on the right panel) due to coannihilation. A few benchmark points are indicated in Table 3 to show the effect of relaxing the case for scalar DM in presence of S_H for $m_{N_1} > m_S$. They should be contrasted with those in Table 2.

BPs	$\{m_{N_1}, m_S, m_{S_H}, \lambda_{SH}, \lambda_{CH}, Y_2, \sin \theta\}$	Δm	$\Omega_{N_1} h^2$	$\Omega_S h^2$	$\left(\frac{\Omega_{N_1} h^2}{\Omega_{DM} h^2}\right) \sigma_{N_1}^{SI}$ (in cm^2)	$\left(\frac{\Omega_S h^2}{\Omega_{DM} h^2}\right) \sigma_S^{SI}$ (in cm^2)
BPB1	{200, 150, 205, 0.006, 0.8, 0.7, 0.01}	50	0.1144	0.0030	9.7×10^{-49}	3.3×10^{-49}
BPB2	{202, 118, 131, 0.002, 0.3, 0.9, 0.04}	101	0.0303	0.0838	7.2×10^{-47}	1.5×10^{-48}
BPB3	{183, 113, 135, 0.009, 0.8, 0.8, 0.04}	201	0.0462	0.0680	1.2×10^{-46}	3.0×10^{-47}
BPB4	{310, 153, 203, 0.052, 0.6, 0.7, 0.02}	300	0.1112	0.0100	2.0×10^{-47}	5.8×10^{-47}
BPB5	{424, 91, 109, 0.004, 0.6, 1.1, 0.03}	503	0.0238	0.0945	2.7×10^{-47}	1.1×10^{-47}

Table 3: Benchmark points allowed by relic density, direct search and invisible Higgs decay limit in presence of a heavy scalar S_H . Input parameters (masses and couplings), relic densities of individual components and direct search cross-sections are mentioned. All the masses are in GeVs.

6 Collider searches at LHC

Collider signature of this model includes searches for scalar and fermion DM. The scalar DM sector doesn't give any novel signature being comprised only of a singlet. Only possible signature can be the production of S through Higgs portal coupling associated with initial state radiation (ISR), yielding mono jet/mono-X signal (higher jet multiplicity can occur suppressed by further jet radiation) plus missing energy [45]. Given the limit on the Higgs portal coupling (λ_{SH}) and DM mass set by the relic density and direct search bound of the model, even in the two component set up, the signal cross-section is very weak to probe anything at near future run of LHC given a huge SM background for such final states³. On the other hand, fermion DM consisting of an admixture of vector-like singlet and doublet leptons, has better prospect of getting unravelled at LHC. This is of particular interest due to the possibility of producing the charged companions of fermion doublet ($N^+ N^-$) at LHC. They eventually decay to DM with off/on-shell W mediation to leptonic final states to yield opposite sign dilepton plus missing energy as pointed out in the left side of Fig. 19. Therefore our interest lies in :

$$\text{Signal} : \ell^+ \ell^- + (\cancel{E}_T),$$

where ℓ includes electrons and muons⁴. However, the detectability of such a signal depends on the effective reduction of corresponding SM background contribution. We will discuss

³Even though the presence of a heavy scalar S_H adds to the freedom of choosing a larger span of scalar DM mass, the strength of the cross-section still is determined by the small λ_{SH} .

⁴Tau detection is harder due to hadronic decay modes.

below how the presence of a second (lighter) DM component as considered in this model framework, enhance the possibility of detecting such signals at LHC. Similar signal events appear for different other models, see for example [46, 47].

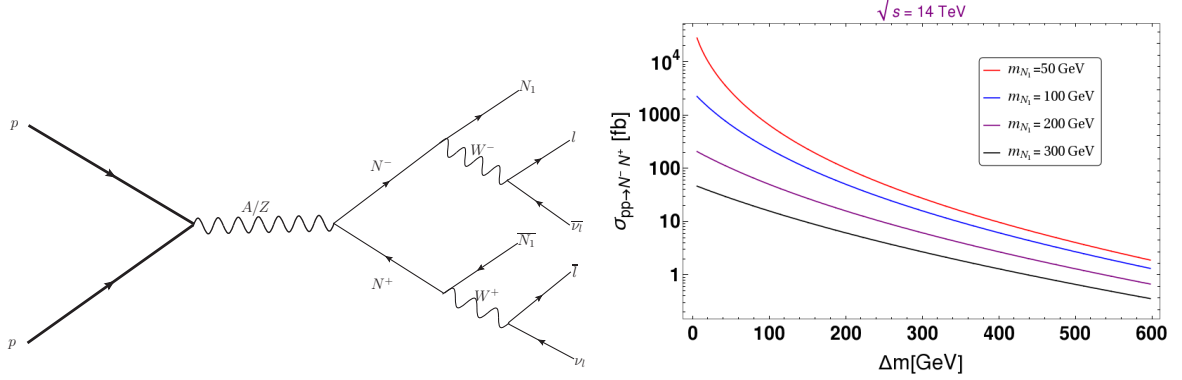


Figure 19: [Left] Feynman diagram for signal process $pp \rightarrow N^+ N^-$, resulting in hadronically quiet opposite sign dilepton plus missing energy ($\ell^+ \ell^- + (\cancel{E}_T)$) events. [Right] Variation in production cross section, $\sigma_{pp \rightarrow N^+ N^-}$ with Δm ($= m_{N^\pm} - m_{N_1}$) for different values of DM mass m_{N_1} [mentioned at figure inset] for centre-of-mass energy $\sqrt{s} = 14$ TeV at LHC.

Signal strength is mainly dictated by the production cross-section for $pp \rightarrow N^+ N^-$ at LHC. This cross-section is essentially a function of m_{N^\pm} and is independent of mixing angle $\sin \theta$. Therefore, one can recast the cross-section as a function of Δm for a fixed DM mass (Given $m_{N^\pm} = m_N + \Delta m$). This is shown in the right panel of Fig. 19 for some different fixed DM masses (mentioned in the figure inset) with centre-of-mass-energy $\sqrt{s} = 14$ TeV. Essentially, this is to show that production cross-section is a falling function of charged fermion masses, but, as Δm plays a crucial role in further decay of the produced charged fermions, we have chosen such parametrisation. We already elaborated that even in the two component set up, direct search crucially tames $\sin \theta \leq 0.1$, it is important to choose a process which is not suppressed by small mixing angle. Therefore, this is the only process of interest. However, also note that, we do not consider the production of heavy neutral fermion N_2 in this analysis (although some of the processes like $N^\pm N_2$ are not suppressed by small $\sin \theta$), which decays through neutral current (Z mediation) interaction to DM N_1 with 100 percent branching ratio. But such signals will be completely washed out by the invariant mass-cut of the leptons not to lie within Z -mass window, that we must apply to suppress SM background (as explained shortly). There are two kinematic constraints that we obey for characteristic collider signal that we discuss here: (i) $m_{\chi_2} > m_{N_1} + m_S$ and (ii) $m_{N_1} > m_S$. The second constraint allows us to choose a large Δm as explained earlier and plays an important role in separating the signal from SM background. Most of the benchmark points in Table 2 and all in Table 3, follow the characteristics mentioned above. We will analyse signal strength for some such benchmark points. Although, we use

benchmark points from Table 2 here, they can also be thought as similar points (with same Δm) from Table 3, where we have further relaxation on scalar DM mass (which do not play a role in the collider signature for fermion DM).

Before getting into the collider analysis, let us briefly explain the experimental environment of LHC, which mainly involves identification of leptons, jets and unclustered objects. Some important variables are also used in the analysis such as missing energy, invariant mass of the dilepton in the final state and scalar sum of the transverse momentum of all the visible objects in the final state. They are identified as follows:

- *Lepton ($l = e, \mu$):* Leptons are identified with a minimum transverse momentum $p_T > 20$ GeV and pseudorapidity $|\eta| < 2.5$. Although the present sensitivity of the detector allows further soft leptons to be identified, we find that such a p_T cut also helps to tame SM background. Leptons require to be isolated if their mutual distance in the $\eta - \phi$ plane is $\Delta R = \sqrt{(\Delta\eta)^2 + (\Delta\phi)^2} \geq 0.2$, while the separation with a jet requires $\Delta R \geq 0.4$.
- *Jets (j):* Jets are formed for simulated signal and background events using cone algorithm PYCELL inbuilt in Pythia event generator. All the partons within $\Delta R = 0.4$ from the jet initiator cell are included to form the jets. We require $p_T > 20$ GeV for a clustered object to be identified as jets in hadron calorimeter (HCAL). Jets are isolated from unclustered objects with $\Delta R > 0.4$. Note here, that although jets are not present in the final state, we require a specific jet identification criteria to demand the final state has zero jets.
- *Unclustered Objects:* All the final state objects with low p_T , which are neither clustered to form jets, nor passes through the identification criteria to become isolated leptons, belong to such category. Hence all particles with $0.5 < p_T < 20$ GeV and $2.5 < |\eta| < 5$, are considered as unclustered objects. They only contribute to missing energy.
- *Missing Energy (E_T):* The transverse momentum of all those electromagnetic charge neutral particles not registered in the detector, can be estimated from the momentum imbalance in the transverse direction associated to the visible particles. Thus missing energy (MET) is defined as:

$$E_T = -\sqrt{\left(\sum_{\ell, j, unc.} p_x\right)^2 + \left(\sum_{\ell, j, unc.} p_y\right)^2}, \quad (6.1)$$

where the sum runs over all visible objects that include the leptons and jets, and the unclustered components. Missing energy is the most significant variable to identify DM at collider.

- *Effective Mass (H_T):* Effective mass of an event is identified here with the scalar sum of the transverse momentum of detectable objects in an event, namely lepton and jets

as follows:

$$H_T = \sum_{\ell,j} (p_T)_{\ell,j} . \quad (6.2)$$

Effective mass usually also includes missing energy as a component added in the scalar sum. However, here we use H_T without including E_T , as we will use E_T as a separate variable in combination of H_T cut anyway to segregate signal from SM background.

- *Invariant mass ($m_{\ell\ell}$):* Invariant mass of opposite sign dilepton is an important variable to segregate SM background from the signal, as it hints to the parent particle mass from which the leptons have been produced. This is defined as:

$$m_{\ell\ell} = \sqrt{(\sum_{\ell} p_x)^2 + (\sum_{\ell} p_y)^2 + (\sum_{\ell} p_z)^2} . \quad (6.3)$$

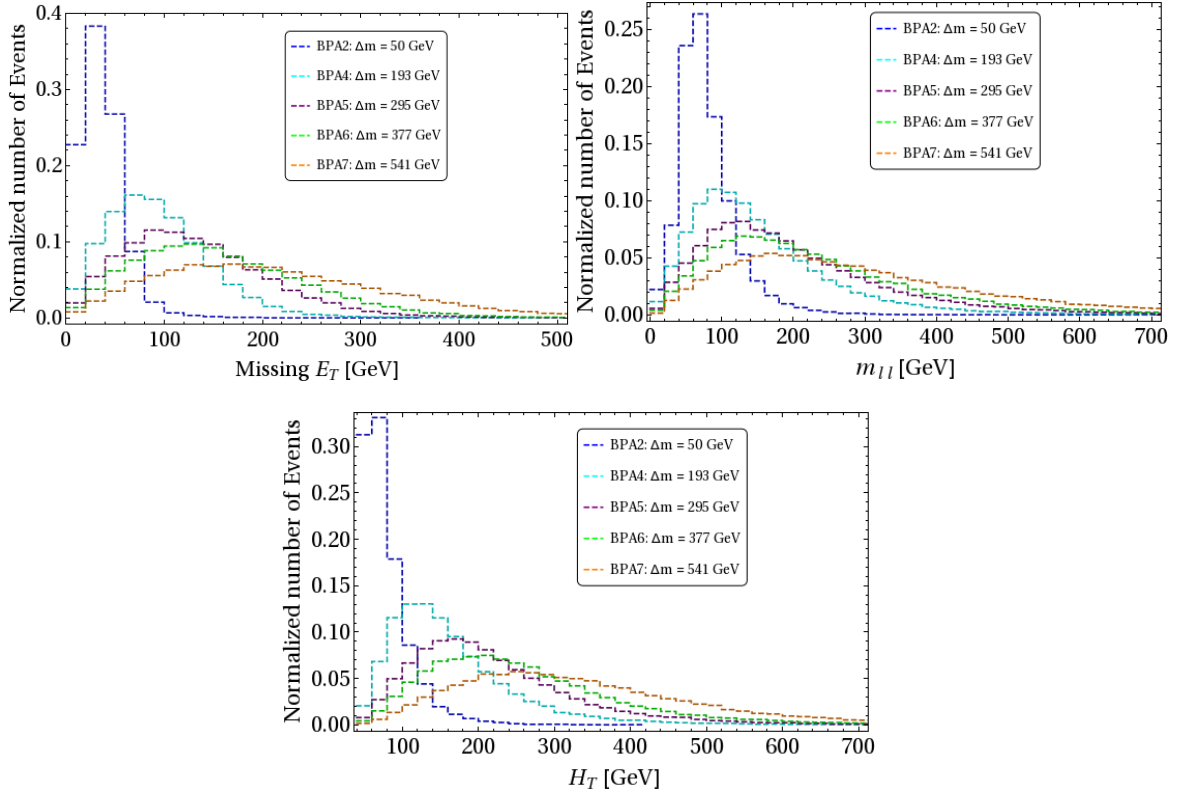


Figure 20: Missing energy (E_T), invariant mass of dilepton ($m_{\ell\ell}$) and effective mass (H_T) distributions of $\ell^+\ell^- + (\cancel{E}_T)$ events from signal at LHC are shown at $\sqrt{s} = 14$ TeV. We have chosen different values of Δm corresponding to different benchmark points as indicated in Table 2.

We inserted the model in `Feynrules` [48] and passed to `Madgraph` [49] to generate signal events, which were further analysed in `Pythia` [50] to reconstruct leptons, jets and

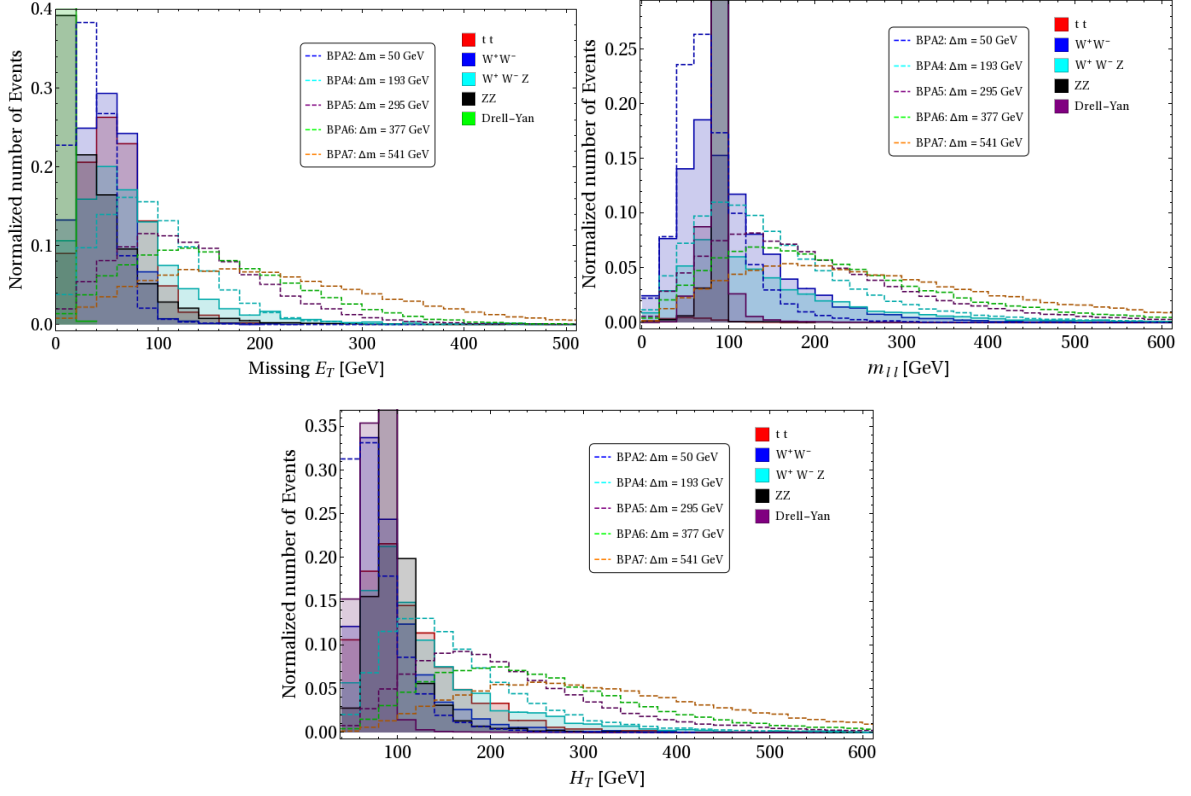


Figure 21: Missing energy (\cancel{E}_T), invariant mass of dilepton ($m_{\ell\ell}$) and effective mass (H_T) distributions of $\ell^+\ell^- + (\cancel{E}_T)$ events from signal (Benchmark points as in Table 2) and dominant SM background events at LHC with $\sqrt{s} = 14$ TeV .

other variables discussed above. The dominant SM backgrounds have been generated in *Madgraph* [49] and then showered through *Pythia* [50]. We have identified dominant SM backgrounds for hadronically quiet opposite sign dilepton events as the production of: $t\bar{t}$, W^+W^- , $W^\pm Z$, ZZ , W^+W^-Z and *Drell-Yan*. We have also used appropriate K -factors to incorporate the Next-to-Leading order (NLO) cross section for the backgrounds. The K -factors chosen are as [51] for $t\bar{t}$: $K = 1.47$, WW : $K = 1.38$, WZ : $K = 1.61$, ZZj : $K = 1.33$, *Drell-Yan* : $K = 1.2$. We have used CTEQ 6L [52] parton distribution function and subprocess centre-of-mass-energy ($\sqrt{\hat{s}}$) as jet energy scale for the analysis.

BPs	Δm (GeV)	$\sigma_{pp \rightarrow N^+ N^-}$ (fb)	\cancel{E}_T (GeV)	H_T (GeV)	σ^{OSD} (fb)	$N_{\text{eff}}^{\text{OSD}}$
BPA2	50	1.73	>100	>100	0.002	< 1
				>200	0.001	< 1
				>300	0.00	0
BPA3	101	6.23	>100	>100	0.155	15
				>200	0.045	4
				>300	0.013	1
			>200	> 100	0.006	1
				>200	0.005	< 1
				>300	0.004	< 1
BPA4	193	2.47	>100	>100	0.305	30
				>200	0.138	14
				>300	0.044	4
			>200	> 100	0.032	3
				>200	0.031	3
				>300	0.017	2
BPA5	295	0.54	>100	>100	0.113	11
				>200	0.075	7
				>300	0.031	3
			>200	> 100	0.032	3
				>200	0.031	3
				>300	0.016	2
			>300	> 100	0.006	1
				>200	0.006	1
				>300	0.005	< 1
BPA6	377	0.27	>100	>100	0.067	7
				>200	0.052	5
				>300	0.027	3
			>200	> 100	0.027	3
				>200	0.027	3
				>300	0.016	2
			>300	> 100	0.007	1
				>200	0.007	1
				>300	0.006	1
BPA7	541	0.06	>100	>100	0.017	2
				>200	0.015	1
				>300	0.011	1
			>200	> 100	0.011	1
				>200	0.010	1
				>300	0.008	1

Table 4: Signal events for few selected benchmark points (BPA2-BPA7, see Table 2) with $\sqrt{s} = 14$ TeV at the LHC for the luminosity $\mathcal{L} = 100 \text{ fb}^{-1}$ after \cancel{E}_T , H_T and $m_{\ell\ell}$ cuts.

SM Backgrounds	$\sigma_{p \rightarrow SM}$ (fb)	\cancel{E}_T (GeV)	H_T (GeV)	σ^{OSD} (fb)	$N_{\text{eff}}^{\text{OSD}}$
$t \bar{t}$	814.78×10^3	>100	>100	17.11	1711
			>200	2.44	244
			>300	< 0.81	< 1
		>200	> 100	< 0.81	< 1
			>200	< 0.81	< 1
			>300	< 0.81	< 1
		>300	> 100	< 0.81	< 1
			>200	< 0.81	< 1
			>300	< 0.81	< 1
$W^+ W^-$	100.06×10^3	>100	>100	20.51	2051
			>200	10.01	1001
			>300	2.00	200
		>200	> 100	2.00	200
			>200	2.00	200
			>300	0.50	50
		>300	> 100	< 0.50	< 1
			>200	< 0.50	< 1
			>300	< 0.50	< 1
$Z Z$	14.03×10^3	>100	>100	0.21	21
			>200	0.14	14
			>300	0.07	7
		>200	> 100	< 0.07	< 1
			>200	< 0.07	< 1
			>300	< 0.07	< 1
		>300	> 100	< 0.07	< 1
			>200	< 0.07	< 1
			>300	< 0.07	< 1
$W^+ W^- Z$	0.16×10^3	>100	>100	0.17	17
			>200	0.09	9
			>300	0.03	3
		>200	> 100	0.04	4
			>200	0.04	4
			>300	0.02	2
		>300	> 100	0.01	1
			>200	0.01	1
			>300	0.01	1

Table 5: Dominant SM background contribution to $\ell^+\ell^- + (\cancel{E}_T)$ signal events with $\sqrt{s} = 14$ TeV at the LHC for luminosity $\mathcal{L} = 100 \text{ fb}^{-1}$ after \cancel{E}_T , H_T and $m_{\ell\ell}$ cuts. The variation of effective number of final state background events with cut-flow are also tabulated.

Most important outcome of this analysis is summarised in Fig. 20, where the distribution of the signal events with respect to \cancel{E}_T , $m_{\ell\ell}$ and H_T are shown in top left, top right and bottom panel. We have chosen different Δm (from the benchmark points as in Table 2) upto as large as ~ 500 GeV allowed by relic density and direct search for illustration. In top left figure, we see that with larger Δm , missing energy distribution becomes flatter and the peak shifts to a higher value. When this is contrasted with the same distributions from those of SM background contributions as pointed out in Fig. 21, we see that the separation of signal events from those of the background becomes easier at high Δm . Therefore, for signal events with large Δm can survive a large \cancel{E}_T cut while reducing the SM background significantly. This should be contrasted with low Δm (~ 50 GeV, BPA2 case), where the peak of missing energy falls within the same ballpark as those of SM backgrounds and therefore can not be separated. Therefore even if the signal cross-section is higher for such cases (as in the single component fermion DM case), the events are submerged into SM background. This feature is not very difficult to understand. With $\Delta m < m_W$, the W decay is off-shell and N^\pm momenta is shared amongst all the final state particles yielding a missing energy peak at lower value. For $\Delta m > m_W$, W is produced on-shell and dominant momenta is carried by the dark matter (N_1) as $m_{N_1} > m_W$. The higher the Δm is, the higher is the available momenta for DM. This therefore yields missing energy peak at larger values with larger mass splitting Δm . We also note that such distinction is also possible with H_T distribution. Again, the larger the Δm , the larger will be the available momenta for the leptons as well. Therefore, large H_T cut can also reduce SM background retaining signals particularly for benchmark points with higher Δm . On the other hand, invariant mass cut can effectively reduce SM background events coming from ZZ and WZ background, when a cut is applied within the Z mass window where the peak of the distribution lies. Therefore, to eliminate SM background from the signal event, we further employ some combination of the following cuts:

- $m_{\ell\ell} < |m_z - 15|$ and $m_{\ell\ell} > |m_z + 15|$,
- $H_T > 100, 200, 300$ GeV,
- $\cancel{E}_T > 100, 200, 300$ GeV.

Signal events with $\Delta m = \{50, 101, 193, 295, 377, 541\}$ GeV corresponding to benchmark points BPA2, BPA4-BPA7 (as in Table 2), are summarised in Table 4, where the cut flow with different H_T and \cancel{E}_T are furnished. The final state event rates (N_{eff}) at a desired luminosity \mathcal{L} is computed by:

$$N_{eff} = \frac{\sigma_p n}{N} \times \mathcal{L}, \quad (6.4)$$

where N is the simulated number of events and n is the obtained final state events corresponding to production cross-section of σ_p . We see that although with larger Δm , the production cross-sections get diminished by the phase space suppression (as already pointed out in RHS of Fig. 19), the shift in the peak of the distribution compensates it to ensure the survival of more number of signal events for such cases. With $\Delta m = 101$ GeV, the

combination of $\cancel{E}_T > 200$ GeV and $H_T > 100$, leaves with a very few events to be observed. $\mathcal{L} = 100 \text{ fb}^{-1}$ turns out to be rather low to see the signals from such events and we need higher luminosity. The main take however is to note that only those cases where Δm is large, has a prospect of discovery by reducing SM background through effective cuts, while those with small Δm as in the single component framework is almost hopeless. The signal event rates can be contrasted with the SM background events with similar cut flow at 14 TeV at LHC as detailed in Table 5. We also note that the limitation in warranting any final state event with number of simulated points yield a limit on the effective background cross-section as indicated in the Table. We see that the dominant SM backgrounds can be tamed down significantly with a combination of \cancel{E}_T and H_T cut. The reach of the signal significance $\sigma = \frac{S}{\sqrt{S+B}}$ is plotted with integrated luminosity \mathcal{L} for selected benchmark points with two different combinations of \cancel{E}_T and H_T cut in left and right panel of Fig. 22. It shows that 5σ significance can be reached with luminosity as high as $\sim 10^4 \text{ fb}^{-1}$.

We also note here that small Δm along with small $\sin \theta$ predicts a delay in the decay of the charged fermion, yielding displaced vertex or stable charge track signature and serves as a characteristic signal for the fermion dark sector with singlet-doublet mixing, as has already been noted in ref. [35]. However, in that case, signal excess in dilepton channel can not be seen. On the contrary, with large Δm , when excess in opposite sign dilepton events can be seen, the decay of the charged fermion is quick and therefore no displaced vertex signature can be observed. Therefore the signal of singlet-doublet fermion DM in presence of a second lighter DM component has a complementarity to that of the same DM in a single component framework as far as collider search is concerned. The presence of a heavy scalar (as illustrated in Sec. 5) doesn't of course change the fermion DM signal discussed here, but allows one to choose the scalar DM in a large mass range.

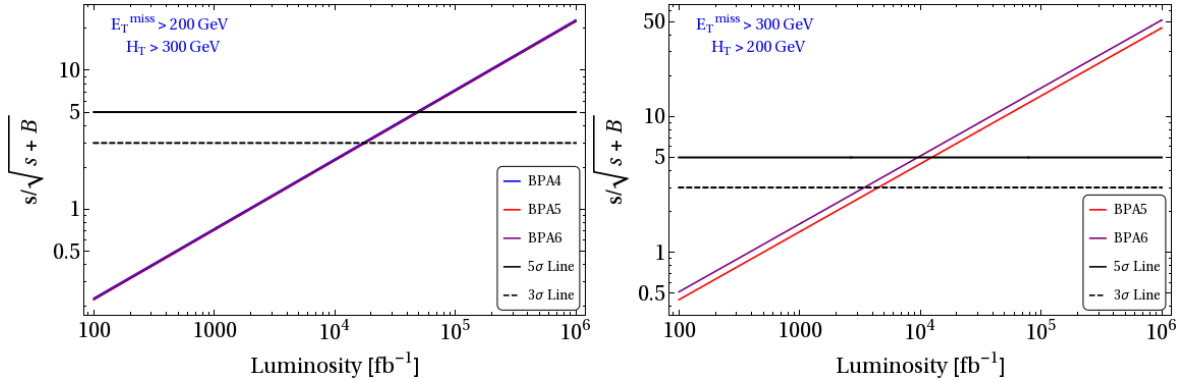


Figure 22: Signal significance $\sigma = \frac{S}{\sqrt{S+B}}$ of OSD events for select few benchmark points (see Table 2) at LHC with $E_{CM} = 14$ TeV as a function of integrated luminosity. Different combinations of \cancel{E}_T , H_T cuts are chosen in left and right panel (mentioned in inset). 3σ (black dashed) and 5σ (black thick) lines are indicated as references.

7 Possible implications to Inflation and Reheating

In this section, we comment briefly on the possibility of production of dark sector particles in the early Universe. It is usually assumed that the early Universe has gone through a period inflation driven by a scalar field, the so called inflaton. Subsequently the inflaton decays perturbatively (nonperturbatively) to bring back a thermal bath, the so called reheating (preheating) phase, with a temperature $T_R > 4$ MeV to pave a path for Big-Bang nucleosynthesis (BBN). See for a review [53, 54]. During the reheating (preheating) phase all the elementary particles, including dark sector, are assumed to be produced. The process of reheating is quite model dependent and accordingly the temperature T_R of thermal bath is set in a large range.

It has been pointed out that during Inflation, the SM Higgs boson may develop a non-zero and large vev $h_I \sim H_I$ [55], where H_I is the Hubble scale at the end of inflation. Therefore, the particles which couple to the Higgs will also acquire very high mass during this period. This may result in a kinematic blocking of the inflaton decay if the mass of the inflaton is lighter than the decay products induced by the non-zero Higgs vev [55]. The phenomena is involved and model dependent. We just provide a brief sketch of the main idea. The presence of the scalar DM which couples to Higgs in our scenario through Higgs portal, may add to the phenomena. A simple illustration of the above situation can be made by looking into the perturbative inflaton decay neglecting backreaction. If we assume a simple inflaton (ϕ) potential given by $V_\phi = m_\phi^2 \phi^2 / 2$, the perturbative reheating temperature (T_R) is obtained through the solution of the following coupled Boltzmann Equations:

$$\begin{aligned}\dot{\rho}_\phi + 3H\rho_\phi &= -\Gamma_\phi \rho_\phi, \\ \dot{\rho}_R + 3H\rho_R &= \Gamma_\phi \rho_\phi,\end{aligned}\tag{7.1}$$

where ρ_ϕ is the density of the inflaton and ρ_R is the density of radiation resulting from the decay of the inflaton with decay width Γ_ϕ . H is the Hubble constant with $H^2 = \frac{8\pi}{3}(\rho_\phi + \rho_R)$. In presence of the DM, the inflaton also decays to DM in addition to SM particles and the total decay width is given by:

$$\Gamma_\phi = \Gamma_0 \left(1 - \frac{4m_f^2}{m_\phi^2}\right)^{3/2} \Theta(m_\phi^2 - 4m_f^2) + \Gamma_0 \left(1 - \frac{4m_s^2}{m_\phi^2}\right)^{3/2} \Theta(m_\phi^2 - 4m_s^2).\tag{7.2}$$

In above equation, for simplicity, we just incorporate the decay to SM fermions (f) and to the scalar DM S . Γ_0 denotes the decay width at zero mass limit. The mass term for the SM fermion and DM are generated from Yukawa interactions (y and λ_{SH}) followed by the large vev (h_I) that Higgs acquires during inflation and will be given by:

$$m_f^2 = \frac{1}{2}y^2 h_I^2; \quad m_S^2 = \frac{1}{2}\lambda_{SH}^2 h_I^2.\tag{7.3}$$

The Θ function in Eq.7.2 denotes the phase space blocking. Depending on whichever is lighter between m_f and m_S , the effective blocking condition for the inflaton decay (assuming

$m_S < m_f$) reads:

$$\frac{h_I^2}{m_\phi^2} > \frac{1}{2\lambda_{SH}^2}. \quad (7.4)$$

As a result the reheating temperature T_R can drop significantly and can be even be less than the Higgs mass depending on the coupling and vev. The delay in reheating may alter the CMB spectrum in terms of the spectral index of density perturbation (n_s) and tensor-to-scalar ratio (r) or affect the heavy particle production. However, one should note here that the maximum temperature T_{\max} during reheating can be much larger than reheating temperature T_R . During reheating, the temperature rises to T_{\max} and then falls to T_R , see for example, [56]:

$$T_{\max} = 0.6g_*^{-1/4}(\Gamma_\phi M_{Pl})^{1/4}M_I^{1/2}, \quad (7.5)$$

where $M_I = V_I^{1/4}$, V_I depicts the energy density at t_{osc} . Depending on the model, maximum temperature can be as high as $T_{\max} \sim 10^3 T_R$. As a result, the heavy particles (including dark sector particles χ_1, χ_2, N, S etc.) in general can be produced during reheating phase itself. Once these particles are produced, irrespective of their initial number density, they can easily thermalise due to their coupling with the SM Higgs and other SM particles. For instance in our case N is a doublet. So it can be easily thermalise due to its gauge coupling. On the other hand, χ_1 , and S are singlet under the SM gauge group. However, these particles couple to the SM Higgs through (large) Yukawa interaction (Y_1 and λ_{SH} respectively). Therefore, the dark sector particles in our case are no more in danger being over produced even if the kinematic blocking effects in a lower reheat temperature as discussed above.

8 Summary

The dark sector of the universe is still a mystery to us. In this work, we have discussed a possible two component (WIMP-like) DM scenario with a vector like fermion (an admixture of a singlet and a doublet) and a scalar singlet stabilised by $\mathcal{Z}_2 \times \mathcal{Z}_2'$ symmetry. The proposed scenario crucially addresses the possibility of DM-DM interaction between fermion and scalar DM candidates through another heavy vectorlike fermion singlet which acts as mediator. We show that in absence of the mediator (which means the absence of t -channel heavy fermion mediated DM-DM interaction), both fermion and scalar DM components behave like two decoupled single component DMs. This is due to suppressed s-channel Higgs mediated interaction between the DM components. In such a situation, both of the sector turns out to fill up the corresponding under-abundant regions to add to the observed relic density. Although such a non interacting situation satisfy observed DM relic density, the direct search limit (XENON1T) rules-out most of the parameter space, particularly for the scalar DM to a very heavy mass $\gtrsim 1$ TeV. For fermion DM, the necessity of co-annihilation contribution limits the mass difference with the charged doublet component to a small value ($\lesssim 12$ GeV).

However, in presence of a heavy fermion mediated t -channel DM-DM conversion, with moderate values of mediator mass ~ 500 GeV, the freeze out and relic density of DM

components get affected significantly. The change is observed mostly in the relic density of the heavier DM component, which has the liberty of annihilating to the lighter DM, unconstrained by direct search limit; while lighter DM component behaves mostly as in single component framework. So, by allowing DM-DM conversion in the interacting picture, we open up large parameter space allowed by both relic density and direct search bounds which otherwise yields over-abundance in non-interacting cases. For fermion DM (when it is heavier than scalar DM), large Δm regions become allowed, but scalar DM is restricted to the Higgs resonance region. In presence of a heavy scalar, which helps co-annihilating the scalar DM component, allow a larger mass range for scalar DM even when it is lighter than fermion DM. On the other hand, when scalar DM is heavier than fermion DM, DM-DM conversion allows the presence of smaller Higgs portal couplings, hiding the scalar DM from direct search to allow a larger mass range upto TeV and beyond.

The work also demonstrates the importance of DM-DM conversion in seeing signals of a dark sector at LHC in relic density and direct search allowed parameter space. In the model, fermion dark sector is composed of a doublet and a singlet. Hence, the charged companions can be produced at LHC which yields hadronically quiet oppsite sign dilepton events plus missing energy through their decays to fermion DM. However, in a single component framework, relic density and direct search constraints restrict the fermion DM to have a small mass difference with the charged companion (Δm), which makes the signal submerged into SM background. On the contrary, in presence of a lighter DM component and an effective DM-DM conversion, Δm can be large, which can segregate the signal from SM background by a combination of large missing energy and effective mass cuts as detailed in the analysis. The discovery limit of such a signal still might be delayed to an integrated luminosity $\sim 10^4 \text{ fb}^{-1}$.

Acknowledgments : The authors would like to acknowledge discussions with Dr. Nirakar Sahoo, Dr. Debaprasad Maity and Dr. Pankaj Saha. PG would like to thank Dr. Rashidul Islam and Basabendu Barman for fruitful discussions and MHRD, Government of India for research fellowship. SB would like to acknowledge the DST-INSPIRE research grant IFA13-PH-57 at IIT Guwahati.

A Single Component vector-like fermion DM

The freeze-out of N_1 DM is controlled by the annihilation and co-annihilation channels as shown in Fig. 23, 24, 25. This is mainly driven by gauge mediation and Higgs mediation apart from the t -channel heavy fermion (N_2, N^\pm) mediation.

Relic density of vector like fermion DM is then governed by the effective number changing cross-section following [57],

$$\begin{aligned} \langle \sigma v \rangle_{N_1}^{eff} &= \frac{g_1^2}{g_{eff}^2} \langle \sigma v \rangle_{\overline{N_1} N_1} + \frac{2g_1 g_2}{g_{eff}^2} \langle \sigma v \rangle_{\overline{N_1} N_2} \left(1 + \frac{\Delta m}{m_{N_1}} \right)^{\frac{3}{2}} e^{-x \frac{\Delta m}{m_{N_1}}} \\ &+ \frac{2g_1 g_3}{g_{eff}^2} \langle \sigma v \rangle_{\overline{N_1} N^-} \left(1 + \frac{\Delta m}{m_{N_1}} \right)^{\frac{3}{2}} e^{-x \frac{\Delta m}{m_{N_1}}} \end{aligned}$$

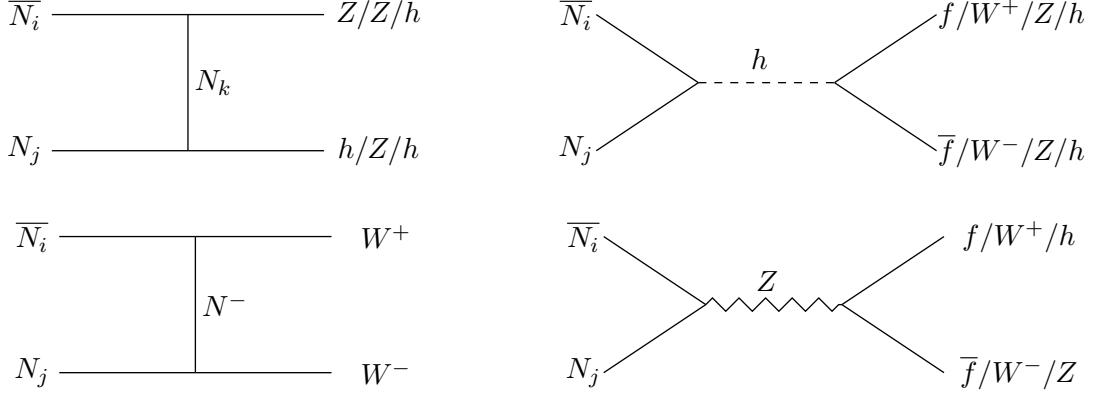


Figure 23: Annihilation ($i = j$) and Co-annihilation ($i \neq j$) of fermion DM. Here $(i, j, k = 1, 2)$.

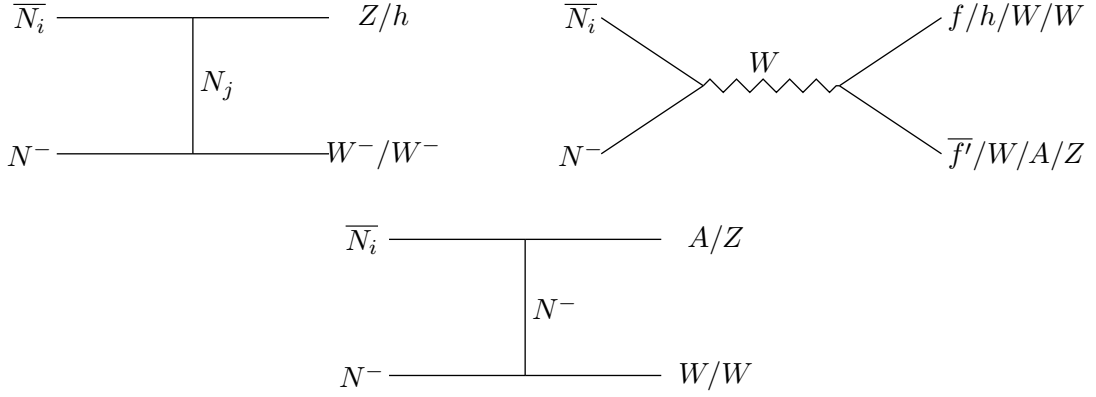


Figure 24: Co-annihilation process of N_i ($i = 1, 2$) with the charge component N^- to SM particles.

$$\begin{aligned}
& + \frac{2g_2g_3}{g_{eff}^2} \langle \sigma v \rangle_{N^+N_2} \left(1 + \frac{\Delta m}{m_{N_1}} \right)^3 e^{-2x \frac{\Delta m}{m_{N_1}}} \\
& + \frac{g_2^2}{g_{eff}^2} \langle \sigma v \rangle_{\bar{N}_2N_2} \left(1 + \frac{\Delta m}{m_{N_1}} \right)^3 e^{-2x \frac{\Delta m}{m_{N_1}}} \\
& + \frac{g_3^2}{g_{eff}^2} \langle \sigma v \rangle_{N^+N^-} \left(1 + \frac{\Delta m}{m_{N_1}} \right)^3 e^{-2x \frac{\Delta m}{m_{N_1}}} .
\end{aligned} \tag{A.1}$$

In above equation, g_{eff} , defined as effective degrees of freedom, is given by

$$g_{eff} = g_1 + g_2 \left(1 + \frac{\Delta m}{m_{N_1}} \right)^{\frac{3}{2}} e^{-x \frac{\Delta m}{m_{N_1}}} + g_3 \left(1 + \frac{\Delta m}{m_{N_1}} \right)^{\frac{3}{2}} e^{-x \frac{\Delta m}{m_{N_1}}} , \tag{A.2}$$

where g_1 , g_2 and g_3 are the degrees of freedom of N_1 , N_2 and N^- respectively and $x = x_f = \frac{m_{N_1}}{T_f}$, where T_f is the freeze out temperature of N_1 . Then relic density will be given

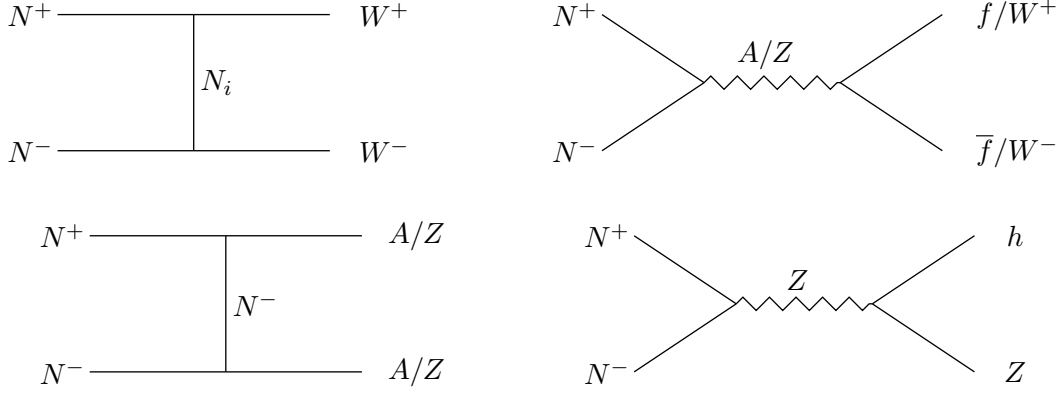


Figure 25: Co-Annihilation process of charged fermions N^\pm to SM particles in final states

by [7, 20] :

$$\Omega h^2 = \frac{854.45 \times 10^{-13}}{\sqrt{106.7}} \frac{x_f}{\langle \sigma v \rangle_{N_1}^{eff}}, \quad (\text{A.3})$$

assuming $x_f \sim 20$.

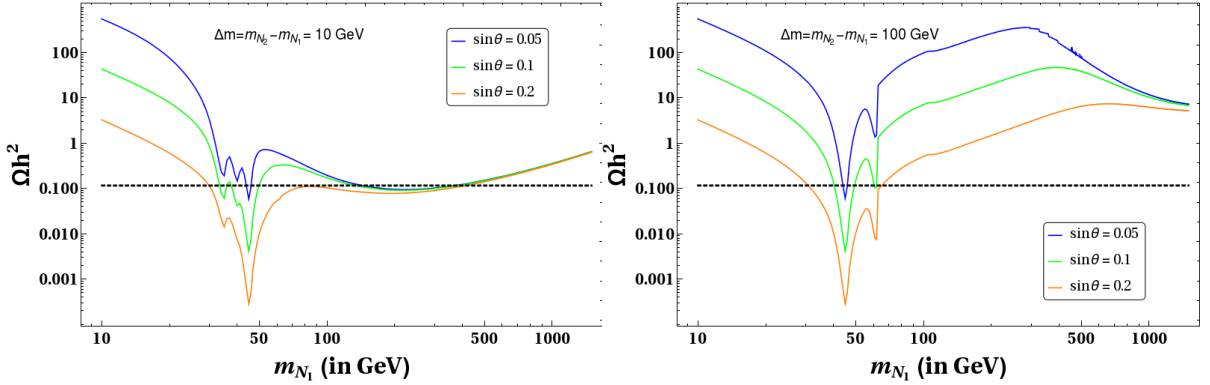


Figure 26: Relic density of N_1 as a function of DM mass, m_{N_1} with different mixing angle, $\sin \theta = 0.05$ (blue), $\sin \theta = 0.1$ (green) and $\sin \theta = 0.2$ (orange). Each plot corresponds to fixed Δm : = 10 GeV (left), 100 GeV (right). Black dashed line indicates observed relic density $0.1133 \leq \Omega_{DM} h^2 \leq 0.1189$.

Variation of relic density of fermion DM is shown as a function of DM mass, for a fixed $\Delta m = 10$ GeV (left panel of the Fig. 26) and 100 GeV (right panel of the Fig. 26) and different choices of mixing angle, $\sin \theta$. We note that the annihilation cross-section is larger when we take larger values of $\sin \theta$, due to larger $SU(2)$ component, resulting smaller relic density. The resonance drop at $m_Z/2$ and at $m_h/2$ is observed due to s -channel Z and H

mediated contributions. For $\Delta m = 100$ GeV, due to smaller co-annihilation contribution relic density increases compared to $\Delta m = 10$ GeV case.

B Higgs Invisible Decay Constraint

When masses of DMs are smaller than the Higgs mass i.e. $m_{DM} < m_h/2$, then Higgs can decay to DM (invisible particles) and will contribute to invisible decay width. LHC data puts strong constraint on the invisible branching fraction of Higgs as $Br(h \rightarrow inv) < 0.24$ [42]. This can be interpreted as follows:

$$\begin{aligned} Br(h \rightarrow inv.) &< 0.24 \\ \frac{\Gamma(h \rightarrow inv.)}{\Gamma(h \rightarrow SM) + \Gamma(h \rightarrow inv.)} &< 0.24, \end{aligned} \quad (B.1)$$

where $\Gamma(h \rightarrow SM) = 4.2$ MeV for SM Higgs (with mass $m_h = 125.09$ GeV) is measured at LHC [42]. This then yields,

$$\Gamma(h \rightarrow inv.) < 1.32 \text{ MeV}. \quad (B.2)$$

In our two component DM scenario, the invisible decay may have two contributions if both m_{N_1} , $m_S < m_h/2$:

$$\Gamma(h \rightarrow inv.) = \Gamma(h \rightarrow \overline{N_1} N_1) + \Gamma(h \rightarrow S S). \quad (B.3)$$

The decay width of Higgs to S and N_1 can easily be calculated as:

$$\begin{aligned} \Gamma_{h \rightarrow S S} &= \frac{\lambda_{SH}^2 v^2}{32\pi m_h^2} \sqrt{m_h^2 - 4m_S^2} \Theta(m_h - 2m_S), \\ \Gamma_{h \rightarrow \overline{N_1} N_1} &= \frac{1}{16\pi} \left(Y_1 \sin 2\theta \right)^2 m_h \left(1 - \frac{4m_{N_1}^2}{m_h^2} \right)^{\frac{3}{2}} \Theta(m_h - 2m_{N_1}). \end{aligned} \quad (B.4)$$

Invisible Higgs decay constraint from Eq. B.2 together with Eq. B.3 and Eq. B.4 is shown in Fig. 27. In top left panel of Fig. 27, the constraint is shown in $m_S - \lambda_{SH}$ plane. Here, the green region is allowed from Higgs invisible decay while grey region excluded for a fixed $\sin \theta = 0.01$. The allowed (or excluded) region remains almost unchanged for any fermion DM mass ($m_{N_1} < m_h/2$) and Δm for the small $\sin \theta$ due to negligible contribution of $\Gamma(h \rightarrow \overline{N_1} N_1)$. In the top right panel we consider larger mixing angle, $\sin \theta = 0.5$. As the contribution the contribution of $\Gamma(h \rightarrow \overline{N_1} N_1)$ plays a important role to $\Gamma(h \rightarrow inv.)$. And therefore, choices of other parameters like m_{N_1} , Δm becomes relevant. The inner region of each contour in $m_S - \lambda_{SH}$ plane (top right panel) is excluded from Higgs invisible decay constraint [42]. Note here however that such large $\sin \theta (= 0.5)$ is disfavoured from direct search bounds [9, 10]. In the bottom panel we have shown excluded region in $m_{N_1} - \sin \theta$ plane keeping other parameters, m_S , λ_{SH} and Δm fixed. Similarly here the inner region of each contour line (which corresponds to different fixed values of Δm and scalar DM mass (m_S), depicted in the figure) is excluded from Higgs invisible decay [42].

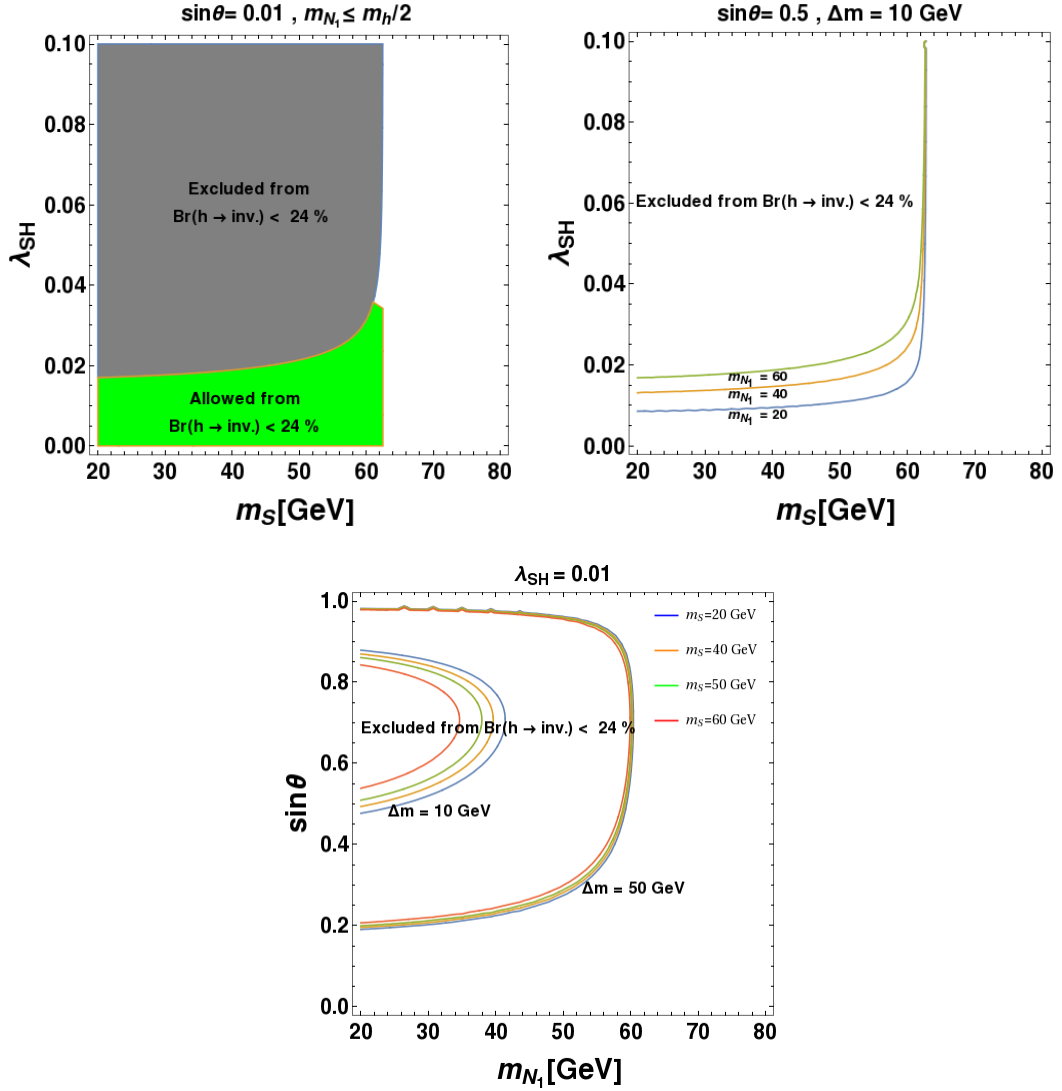


Figure 27: Constraints on scalar and fermion DM from Higgs invisible branching ratio $Br(h \rightarrow inv.) < 0.24$ [42] in $m_S - \lambda_{SH}$ plane (top panel) and $m_{N_1} - \sin \theta$ plane (bottom panel) keeping other parameter fixed (mentioned in the figure inset).

C Invisible Decay Constraint of Z

As the fermion DM has a doublet component in it, it has Z mediated interaction. Hence, if fermion DM mass is below $m_Z/2$, then Z can invisibly decay to dark particles. From current observation, invisible decay width of Z is strongly constrained. The upper limit of invisible Z decay width is following [42]:

$$\Gamma(Z \rightarrow inv.) \leq 499.0 \pm 1.5 \text{ MeV}, \quad (\text{C.1})$$

where in our model,

$$\begin{aligned}\Gamma(Z \rightarrow inv.) &= \Gamma(Z \rightarrow \bar{N}_1 N_1) \\ &= \frac{1}{48\pi} \left(\frac{g \sin^2 \theta}{\cos \theta_W} \right)^2 m_Z \left(1 + \frac{2m_{N_1}^2}{m_Z^2} \right) \sqrt{1 - \frac{4m_{N_1}^2}{m_Z^2}} \Theta(m_Z - 2m_{N_1}) \quad (\text{C.2})\end{aligned}$$

Invisible decay of Z mainly depend on mixing angle $\sin \theta$. Choice of small mixing angle, with $\sin \theta < 0.1$ is preferable from direct search bound in which all fermion DM mass $m_{N_1} < m_Z/2$ is allowed from invisible decay width of Z [20]. We note that as the scalar DM component is a gauge singlet, it doesn't have a Z mediated interaction and therefore no constraint from invisible Z decay applies to it.

References

- [1] V. C. Rubin, *Optical observations of radio galaxies and quasi-stellar objects* *Optical observations of radio galaxies and quasi-stellar radiosources*, in *Hautes Energies en Astrophysique: Proceedings, Ecole d'Eté de Physique Théorique, Les Houches, France, 1966*, vol. 1, pp. 133–152, 1967.
- [2] V. C. Rubin and W. K. Ford, Jr., *Rotation of the Andromeda Nebula from a Spectroscopic Survey of Emission Regions*, *Astrophys. J.* **159** (1970) 379–403.
- [3] W. Hu and S. Dodelson, *Cosmic microwave background anisotropies*, *Ann. Rev. Astron. Astrophys.* **40** (2002) 171–216, [[astro-ph/0110414](#)].
- [4] G. Bertone, D. Hooper and J. Silk, *Particle dark matter: Evidence, candidates and constraints*, *Phys. Rept.* **405** (2005) 279–390, [[hep-ph/0404175](#)].
- [5] WMAP collaboration, G. Hinshaw et al., *Nine-Year Wilkinson Microwave Anisotropy Probe (WMAP) Observations: Cosmological Parameter Results*, *Astrophys. J. Suppl.* **208** (2013) 19, [[1212.5226](#)].
- [6] PLANCK collaboration, P. A. R. Ade et al., *Planck 2013 results. XVI. Cosmological parameters*, *Astron. Astrophys.* **571** (2014) A16, [[1303.5076](#)].
- [7] E. W. Kolb and M. S. Turner, *The Early Universe*, *Front. Phys.* **69** (1990) 1–547.
- [8] J. Billard, L. Strigari and E. Figueroa-Feliciano, *Implication of neutrino backgrounds on the reach of next generation dark matter direct detection experiments*, *Phys. Rev.* **D89** (2014) 023524, [[1307.5458](#)].
- [9] LUX collaboration, D. S. Akerib et al., *Limits on spin-dependent WIMP-nucleon cross section obtained from the complete LUX exposure*, *Phys. Rev. Lett.* **118** (2017) 251302, [[1705.03380](#)].
- [10] XENON collaboration, E. Aprile et al., *Dark Matter Search Results from a One Tonne× Year Exposure of XENON1T*, [1805.12562](#).
- [11] XENON collaboration, E. Aprile et al., *Physics reach of the XENON1T dark matter experiment*, *JCAP* **1604** (2016) 027, [[1512.07501](#)].
- [12] PANDAX-II collaboration, X. Cui et al., *Dark Matter Results From 54-Ton-Day Exposure of PandaX-II Experiment*, *Phys. Rev. Lett.* **119** (2017) 181302, [[1708.06917](#)].
- [13] Q.-H. Cao, E. Ma, J. Wudka and C. P. Yuan, *Multipartite dark matter*, [0711.3881](#).

- [14] S. Bhattacharya, A. Drozd, B. Grzadkowski and J. Wudka, *Two-Component Dark Matter*, *JHEP* **10** (2013) 158, [[1309.2986](#)].
- [15] A. Biswas, D. Majumdar, A. Sil and P. Bhattacharjee, *Two Component Dark Matter : A Possible Explanation of 130 GeV γ - Ray Line from the Galactic Centre*, *JCAP* **1312** (2013) 049, [[1301.3668](#)].
- [16] L. Bian, R. Ding and B. Zhu, *Two Component Higgs-Portal Dark Matter*, *Phys. Lett.* **B728** (2014) 105–113, [[1308.3851](#)].
- [17] S. Esch, M. Klasen and C. E. Yaguna, *A minimal model for two-component dark matter*, *JHEP* **09** (2014) 108, [[1406.0617](#)].
- [18] A. Dutta Banik, M. Pandey, D. Majumdar and A. Biswas, *Two component WIMP-FImP dark matter model with singlet fermion, scalar and pseudo scalar*, *Eur. Phys. J.* **C77** (2017) 657, [[1612.08621](#)].
- [19] M. Klasen, F. Lyonnet and F. S. Queiroz, *NLO+NLL collider bounds, Dirac fermion and scalar dark matter in the B-L model*, *Eur. Phys. J.* **C77** (2017) 348, [[1607.06468](#)].
- [20] S. Bhattacharya, P. Ghosh and P. Poulose, *Multipartite Interacting Scalar Dark Matter in the light of updated LUX data*, *JCAP* **1704** (2017) 043, [[1607.08461](#)].
- [21] S. Bhattacharya, P. Ghosh, T. N. Maity and T. S. Ray, *Mitigating Direct Detection Bounds in Non-minimal Higgs Portal Scalar Dark Matter Models*, *JHEP* **10** (2017) 088, [[1706.04699](#)].
- [22] J. Herrero-Garcia, A. Scaffidi, M. White and A. G. Williams, *On the direct detection of multi-component dark matter: sensitivity studies and parameter estimation*, *JCAP* **1711** (2017) 021, [[1709.01945](#)].
- [23] M. Aoki, D. Kaneko and J. Kubo, *Multicomponent Dark Matter in Radiative Seesaw Models*, *Front.in Phys.* **5** (2017) 53, [[1711.03765](#)].
- [24] N. Khan, *Neutrino mass and the Higgs portal dark matter in the ESSFSM*, *Adv. High Energy Phys.* **2018** (2018) 4809682, [[1707.07300](#)].
- [25] A. Ahmed, M. Duch, B. Grzadkowski and M. Iglicki, *Multi-Component Dark Matter: the vector and fermion case*, [1710.01853](#).
- [26] J. Herrero-Garcia, A. Scaffidi, M. White and A. G. Williams, *Reproducing the DAMA/LIBRA phase-2 results with two dark matter components*, [1804.08437](#).
- [27] M. Aoki and T. Toma, *Boosted Self-interacting Dark Matter in a Multi-component Dark Matter Model*, [1806.09154](#).
- [28] S. Yaser Ayazi and A. Mohamadnejad, *Scale-Invariant Two Component Dark Matter*, [1808.08706](#).
- [29] A. Poulin and S. Godfrey, *Multi-component dark matter from a hidden gauged SU(3)*, [1808.04901](#).
- [30] S. Chakraborti and P. Poulose, *Interplay of Scalar and Fermionic Components in a Multi-component Dark Matter Scenario*, [1808.01979](#).
- [31] J. A. Casas, D. G. Cerdeño, J. M. Moreno and J. Quilis, *Reopening the Higgs portal for single scalar dark matter*, *JHEP* **05** (2017) 036, [[1701.08134](#)].
- [32] J. McDonald, *Gauge singlet scalars as cold dark matter*, *Phys. Rev.* **D50** (1994) 3637–3649, [[hep-ph/0702143](#)].

- [33] P. Ghosh, A. K. Saha and A. Sil, *Study of Electroweak Vacuum Stability from Extended Higgs Portal of Dark Matter and Neutrinos*, *Phys. Rev.* **D97** (2018) 075034, [[1706.04931](#)].
- [34] S. Bhattacharya, N. Sahoo and N. Sahu, *Minimal vectorlike leptonic dark matter and signatures at the LHC*, *Phys. Rev.* **D93** (2016) 115040, [[1510.02760](#)].
- [35] S. Bhattacharya, N. Sahoo and N. Sahu, *Singlet-Doublet Fermionic Dark Matter, Neutrino Mass and Collider Signatures*, *Phys. Rev.* **D96** (2017) 035010, [[1704.03417](#)].
- [36] M. Hoferichter, P. Klos, J. Menéndez and A. Schwenk, *Improved limits for Higgs-portal dark matter from LHC searches*, *Phys. Rev. Lett.* **119** (2017) 181803, [[1708.02245](#)].
- [37] L. Feng, S. Profumo and L. Ubaldi, *Closing in on singlet scalar dark matter: LUX, invisible Higgs decays and gamma-ray lines*, *JHEP* **03** (2015) 045, [[1412.1105](#)].
- [38] S. Bhattacharya, B. Karmakar, N. Sahu and A. Sil, *Flavor origin of dark matter and its relation with leptonic nonzero θ_{13} and Dirac CP phase δ* , *JHEP* **05** (2017) 068, [[1611.07419](#)].
- [39] P. Pal, *An Introductory Course of Particle Physics*. Taylor & Francis, 2014.
- [40] F. Pisano and A. T. Tran, *Anomaly cancellation in a class of chiral flavor gauge models*, in *14th Brazilian Meeting on Particles and Fields Caxambu, Brazil, September 29-October 3, 1993*, 1993.
- [41] K. Kannike, *Vacuum Stability of a General Scalar Potential of a Few Fields*, *Eur. Phys. J.* **C76** (2016) 324, [[1603.02680](#)].
- [42] PARTICLE DATAGROUP collaboration, M. Tanabashi et al., *Review of Particle Physics*, *Phys. Rev.* **D98** (2018) 030001.
- [43] M. Aoki, M. Duerr, J. Kubo and H. Takano, *Multi-Component Dark Matter Systems and Their Observation Prospects*, *Phys. Rev.* **D86** (2012) 076015, [[1207.3318](#)].
- [44] G. Bélanger, F. Boudjema, A. Pukhov and A. Semenov, *micrOMEGAs4.1: two dark matter candidates*, *Comput. Phys. Commun.* **192** (2015) 322–329, [[1407.6129](#)].
- [45] H. Han, J. M. Yang, Y. Zhang and S. Zheng, *Collider Signatures of Higgs-portal Scalar Dark Matter*, *Phys. Lett.* **B756** (2016) 109–112, [[1601.06232](#)].
- [46] S. Bahrami, M. Frank, D. K. Ghosh, N. Ghosh and I. Saha, *Dark matter and collider studies in the left-right symmetric model with vectorlike leptons*, *Phys. Rev.* **D95** (2017) 095024, [[1612.06334](#)].
- [47] B. Barman, S. Bhattacharya and M. Zakeri, *Multipartite Dark Matter in $SU(2)_N$ extension of Standard Model and signatures at the LHC*, [1806.01129](#).
- [48] A. Alloul, N. D. Christensen, C. Degrande, C. Duhr and B. Fuks, *FeynRules 2.0 - A complete toolbox for tree-level phenomenology*, *Comput. Phys. Commun.* **185** (2014) 2250–2300, [[1310.1921](#)].
- [49] J. Alwall, M. Herquet, F. Maltoni, O. Mattelaer and T. Stelzer, *MadGraph 5 : Going Beyond*, *JHEP* **06** (2011) 128, [[1106.0522](#)].
- [50] T. Sjostrand, S. Mrenna and P. Z. Skands, *PYTHIA 6.4 Physics and Manual*, *JHEP* **05** (2006) 026, [[hep-ph/0603175](#)].
- [51] J. Alwall, R. Frederix, S. Frixione, V. Hirschi, F. Maltoni, O. Mattelaer et al., *The automated computation of tree-level and next-to-leading order differential cross sections, and their matching to parton shower simulations*, *JHEP* **07** (2014) 079, [[1405.0301](#)].

- [52] R. Placakyte, *Parton Distribution Functions*, in *Proceedings, 31st International Conference on Physics in collisions (PIC 2011): Vancouver, Canada, August 28-September 1, 2011*, 2011. [1111.5452](#).
- [53] J. Martin, C. Ringeval and V. Vennin, *Encyclopædia Inflationaris*, *Phys. Dark Univ.* **5-6** (2014) 75–235, [[1303.3787](#)].
- [54] J. Martin, *The Observational Status of Cosmic Inflation after Planck*, *Astrophys. Space Sci. Proc.* **45** (2016) 41–134, [[1502.05733](#)].
- [55] K. Freese, E. I. Sfakianakis, P. Stengel and L. Visinelli, *The Higgs Boson can delay Reheating after Inflation*, *JCAP* **1805** (2018) 067, [[1712.03791](#)].
- [56] R. Rangarajan and N. Sahu, *Perturbative Reheating and Gravitino Production in Inflationary Models*, *Phys. Rev.* **D79** (2009) 103534, [[0811.1866](#)].
- [57] K. Griest and D. Seckel, *Three exceptions in the calculation of relic abundances*, *Phys. Rev.* **D43** (1991) 3191–3203.